Experimental and numerical investigation of the thermal properties and related microstructural influences of an interpenetrating metal ceramic composite at elevated temperatures

Joél Schukraft, Dominik Horny, Frederik Siegmund, Katrin Schulz, Kay André Weidenmann

Angaben zur Veröffentlichung / Publication details:

Schukraft, Joél, Dominik Horny, Frederik Siegmund, Katrin Schulz, and Kay André Weidenmann. 2023. "Experimental and numerical investigation of the thermal properties and related microstructural influences of an interpenetrating metal ceramic composite at elevated temperatures." *Thermochimica Acta* 726: 179557. https://doi.org/10.1016/j.tca.2023.179557.

Experimental and numerical investigation of the thermal properties and related microstructural influences of an interpenetrating metal ceramic composite at elevated temperatures

Joél Schukraft [*,a], Dominik Horny [b,c], Frederik Siegmund [a], Katrin Schulz [b,c], Kay André Weidenmann [a]

[a] University of Augsburg, Institute of Materials Resource Management (MRM) Germany
[b] Karlsruhe Institute of Technology (KIT), Institute for Applied Materials - Reliability and Microstructure (IAM-ZM) Germany
[c] Hochschule Karlsruhe - University of Applied Sciences (HKA), Institute of Applied Research (IAF) Germany

1. Introduction

Metal-matrix composites (MMC) have been of interest to researchers for several years, as they promise to close the gap in the material selection between lightweight metals (high specific mechanical properties and good heat conductivity, but low temperature resistance) and ceramics (excellent elastic properties and high operating temperature limits, but brittle behavior). Combining both materials in a composite has majorly improved mechanical stiffness, strength and wear resistance, as well as the coefficient of thermal expansion (CTE) in widespread applications [1]. Examples range from the automotive industry [2] across aerospace applications [3] to electronic components [4]. Here, MMCs have the decisive advantage that they can combine high thermal conductivity and an adjustable CTE which can be exploited for example in heat sinks for high-performance electronic components [5, 6].

Interpenetrating metal-ceramic composites (IMCC), where both phases are continuous, offer an even greater potential than conventional whisker [7], particle [8], fiber [9] or platelet [10] reinforced MMCs [11]. Improved mechanical properties (higher stiffness and strength), enhanced wear-resistance, as well as lower and even taylorable CTEs are reported [12].

Combining two phases interpenetratingly in a composite, rises a number of scientific questions regarding the temperature dependent properties, the build-up of internal stresses during manufacturing and thermal cycling and the influence of residual porosity.

Early studies have already addressed some of these issues, and fundamental findings have been made on the thermal strain and CTE hysteresis between heating and cooling [13], as well as on estimating internal stresses [14] in Al_2O_3/Al interpenetrating phase composites (IPCs) manufactured by pressure infiltration. Thermal expansion of IPCs with similar constituents produced by liquid displacement reaction has been studied by LaVecchia et al. [15]. In a more recent work [16], anisotropies of the CTE behavior in freeze-cast IMCCs have been

* Corresponding author.

https://doi.org/10.1016/j.tca.2023.179557

investigated.

Nevertheless, there are still open questions regarding the mechanisms behind the observed phenomena, that have been answered only partially or not at all. For example, the studies mentioned revealed the importance of the ceramic fraction on the thermal expansion behavior of the IMCC. However, composites with Al_2O_3 fractions < 40 vol% have not been investigated. The influence of porosity was suggested and discussed theoretically by Balch et al. [17] and Skirl et al. [13]. It has been suggested, that pores in the metallic phase contribute to the heating cooling hysteresis of thermal expansion in experimental [4] and numerical [18,19] studies of SiC/Al IPCs with ceramic contents > 55 vol.%. However, a detailed analysis regarding the relevance of porosity on the temperature dependence of the CTE is still missing. Further, the appearance of a peak in the CTE curve during the first heating cycle, as well as the discussion of the CTE cooling curve has not been considered in most studies. Only a few authors present possible explanation approaches (cf. Huber et al. [4]).Advanced investigation methods, as the in-situ SEM with subsequent digital image correlation (DIC) evaluation and the combination of experimental and numerical methods can shed light to the mechanisms of action.

For this purpose, the heat capacity, thermal conductivity and thermal expansion coefficient of an AlSi10Mg/Al_2O_3 interpenetrating metal ceramic composite with an alumina fraction of 26 vol.% as well as the influence of thermal cycling on the microstructure and the effective properties are investigated in this study. Temperature dependent thermal properties are studied in a series of experiments and supplemented by 3D simulations with varying model assumptions. The synergy of advanced experimental and numerical analyses gives insights into the microstructural mechanisms that are relevant to the macroscopic thermal behavior of the IMCC. It further helps to discuss the hypotheses proposed in literature and to answer some of the remaining scientific questions. Finally, cyclic in-situ heating experiments are performed and the evolution of the related, thermally induced stresses is investigated numerically in order to asses the potential of AlSi10Mg/Al_2O_3 IMCCs in operating conditions.

2. Material system

The interpenetrating composite consists of two, continuously connected phases. The ceramic phase is manufactured via mechanical stirring of a stabilized alumina slurry, subsequently dried and sintered. The resulting open-porous ceramic foam is provided by Morgan Advanced Materials Haldenwanger GmbH, who hold a patent on the manufacturing [20]. The metallic phase is infiltrated into the ceramic foam's open-porous, spherical pore structure via gas pressure infiltration. Therefore, a ceramic preform cuboid (approx. $65\,x\,65\,x\,20\,mm^3$) with a steel sinker on top is put into a boron nitride covered crucible, together with slabs of the metallic AlSi10Mg alloy. The crucible is heated up to 700 °C in a gas pressure infiltration system under vacuum with a residual pressure of maximum $2{\cdot}10^{-2}\,mbar$. As the alloy is fully melted and surrounds the evacuated porous alumina foam, argon gas pressure is applied to the melt surface at a pressure of 60 *bar* to infiltrate the aluminum alloy into the open porosity of the ceramic preform. After a dwell time of 10 minutes, the setup is cooled passively to room temperature and the metal solidifies within the ceramic foam under remaining pressure. More details about the manufacturing process, as well as a schematic drawing of the setup can be found in a former publication by the authors [21]. Samples were cut out of the inner of the infiltration block with a diamond wire saw DWS.250, Diamond Wire Tech, Weinheim, Germany and a respective diamond wire of 350 μm diameter.

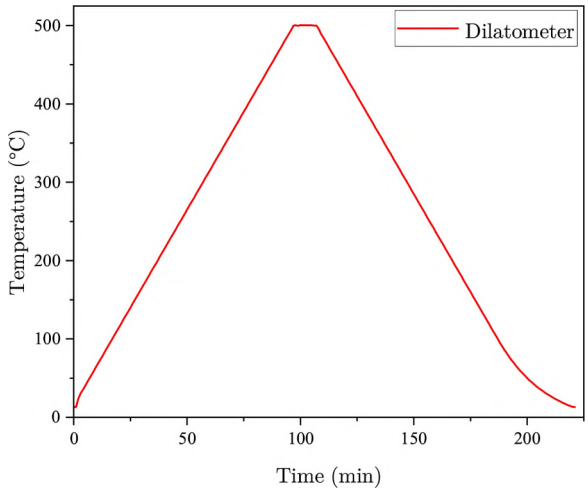

Fig. 1. A representative time-temperature diagram of the experimental captured data for one heating cycle.

The microstructure of the composite shows a mean pore radius of 14.4 μm and a median pore radius of 10.0 μm (compare Horny et al. [21]). The metallic phase infiltrates the accessible open porosity of the ceramic preform and forms precipitations during solidification, regarding the Scheil scheme of AlSi10Mg (compare Mrvar et al. [22] in Vocina et al. [23]). Previous research has shown residual porosity of the composite clearly below 3% [24]. The phase interaction was determined to be strong between ceramic and metal, as soon as complete wetting takes place during manufacturing and sickle-shaped porosity by internal surface detachment could be reduced by increasing the infiltration pressure from 40 to 60 *bar* (compare Horny et al. [21]). Mechanical properties were investigated for elastic modulus in Horny et al. [21] and the temperature dependent elastic modulus in Schukraft et al. [25]. The elastic-plastic behavior of the material system is described and discussed by Schukraft et al. [24,26].

3. Experimental

In the following the experimental procedure of the investigation methods will be presented.

3.1. Dynamic scanning calorimetry

To measure the specific heat capacity C_p of the composite according to equation 1, heat-flux dynamic scanning calorimetry (DSC) was performed using a DSC 214 Polyma, by Netzsch, Selb, Germany.

$$C_p = \frac{\Delta Q}{m{\cdot}\Delta T} \tag{1}$$

If the amount of heat ΔQ is added to or removed from a body, its temperature T changes proportionally. The proportionality factor is composed of the body's mass m and the specific heat capacity. Six samples of about 25 *mg* were heated from 0 to 120 °C with a heating rate of 10 K/min and isothermic holding times of 10 *min* at the beginning and the maximum temperature. 40 ml/min of nitrogen were used as a purge gas. Measurements were conducted according to DIN 51007:2019-04 [27]. A sapphire sample was used for calibration. For comparison, a preform and an AlSi10Mg sample were measured twice each.

3.2. Laser flash analysis

The thermal conductivity λ is a material-specific constant that relates the flow of thermal energy. It is defined as follows [28]:

$$\lambda = a{\cdot}\rho{\cdot}C_p \tag{2}$$

Where a is the thermal diffusivity, ρ is the density, and C_p is the specific heat capacity described in Section 3.1. Thermal diffusivity was measured according to ASTM E1461-13(2022) [28] by a laser flash

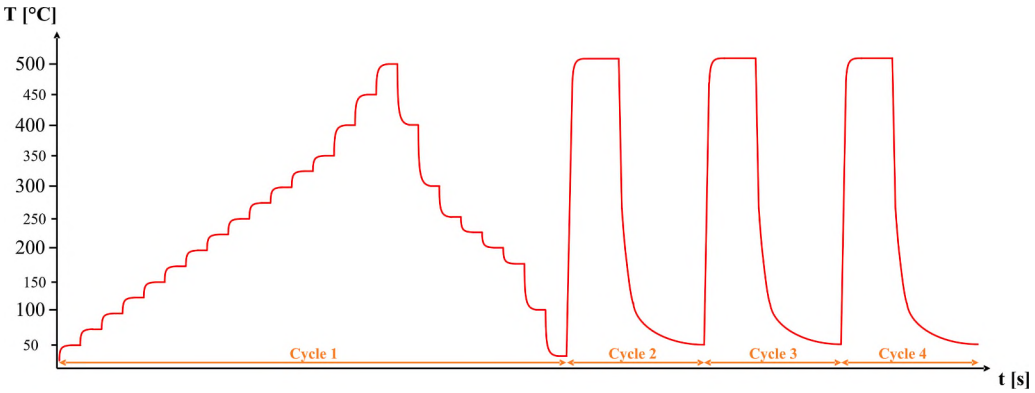

Fig. 2. Schematic time-temperature diagram of the in-situ experiments. For equilibrium conditions at the respective temperature steps, a holding time was set before the images were captured. The first heating cycle was captured in 25 K steps up to 350 °C, followed by 50 K steps up to 500 °C. For cooling the relevant area in the dilatometry curve was investigated in smaller steps. In the cycle 2 to 4, the temperature was captured at 500 and 50 °C, and cycling took approximately 45 min per cycle.

analysis setup LFA 1000 by Linseis, Selb, Germany. Two samples with dimensions of about $20\,x\,20\,x\,3\,mm$ were each measured ten times at room temperature and at 100 °C with a $2\,ms$ trapeze pulse. For comparison an AlSi10Mg sample was also measured ten times.

3.3. Dilatometry

The determination of the CTE was carried out with a Netzsch Dil 402, Selb, Germany, according to DIN 51045:2005-08 [29]. The sample was held between a fixed end and the measuring plunger with a force of $200\,mN$ and in nitrogen atmosphere with a purge rate of $20\,ml\,/min$ during the whole experiment. The heating and cooling rate was set to $5\,K\,/min$ in a range from 0 to 500 °C and a holding time of $10\,min$ was set at the maximum temperature, to stabilize the temperature while a vortex cooler was switched on for a continuous cooling process. To calibrate the equipment, a reference measurement with pure alumina, provided by the manufacturer, was carried out with the planned temperature program. A temperature plot of one thermal cycle is given in Fig. 1, showing a continuous cooling rate down to 50 °C. The cuboid specimen had dimensions of approximately $25\,x\,5\,x\,5\,mm^3$. Data of the length change ($dL\,/L_0$), temperature, time and contact force of the measuring plunger were recorded with the length of the specimen at room temperature $L_0 = L(T = 25\,^\circ\mathrm{C})$. The differential coefficient of thermal expansion (CTE) is subsequently determined by the temperature derivative of the thermal strain:

$$\alpha_{th}(T) = \mathrm{CTE}(T) = \frac{dL}{L_0}\frac{d}{dT} \tag{3}$$

Three aluminum alloy samples with the same thermal history as the infiltrated IMCC, three ceramic preform samples and seven IMCC samples were measured three times and the average was calculated and plotted for each cycle. For the investigation of the material behavior under cyclic heating, three IMCC samples were measured for six further heating cycles.

3.4. In-situ scanning electron microscopy experiments

To investigate the microstructure of the sample during heating and cooling, as well as at certain temperature steps, a tensile-compression in-situ module with a heating unit by Kammrath&Weiss, Schwerte, Germany, was used in a Quattro ESEM by Thermofisher Scientific, Waltham, USA, located at the German Aerospace Center, Institute of Test and Simulation for Gas Turbines, Augsburg. Temperature controlling unit TDS and force-displacement controlling unit DDS4, each also by Kammrath&Weiss were used. Samples were cut into cuboids with dimensions of $50\,x\,5\,x\,2\,mm^3$, grinded with SiC abrasive paper of grade *P*800 and finally polished on one side for microstructural investigation. Four polishing steps were used on a Tegramin 25, by Struers, Ballerup, Denmark, described in detail by Wegscheider et al. [30]. The experiments were carried out force controlled with $0\,N$ and the temperature, force and elongation (measured at the crosshead of the setup with an linear encoder) were tracked. High-resolution images were captured at three different positions at every temperature step and one overview image of the relevant sample section was recorded. The time-temperature plot is given in Fig. 2. Acceleration voltage was chosen to $10\,kV$, beam current to approx. $100\,pA$, a spot size of 3.5 and a capturing time of $45\,\mu s$ in the secondary electron mode with an ETD detector. The scale bar is given in each image. The software ARAMIS Professional from GOM Correlate, Braunschweig, Germany was used to evaluate the strain field on the sample surface. Therefore, the SEM images were imported into the software with a resolution of 1536 x 1094 pixels. The facet size was chosen to 31 pixels and the dot pitch to 16 pixels respective the microstructural surface pattern and a pixel length of $675\,nm$ within the images.

4. Modeling

4.1. Basic model

Numerical investigations are performed on 3D cubic volume elements (VEs) of the IMCC with an overall ceramic volume fraction of 26% and a representative size according to [21]. Both reconstructed and generated microstructures are used for the geometrical representation (cf. Fig. 5). These representative volume elements (RVEs) are subjected to an in-phase heating and cooling in a range of $25 - 500\,^\circ\mathrm{C}$. Due to the low experimental heating and cooling rates, spatial variations in the temperature field are neglected and a uniform temperature throughout the volume element is assumed. In some analyses an initial cooling from a temperature T_0 is added before the first heating. For clarity, the respective temperature profiles are shown in Fig. 3.

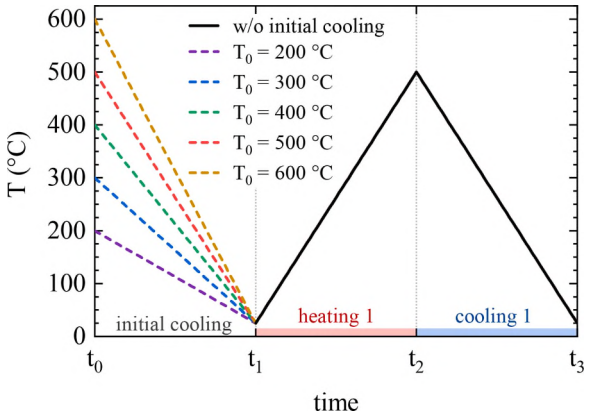

Fig. 3. Temperature profiles of the numerical investigations. First heating and cooling cycle without and with initial cooling from different initial temperatures T_0.

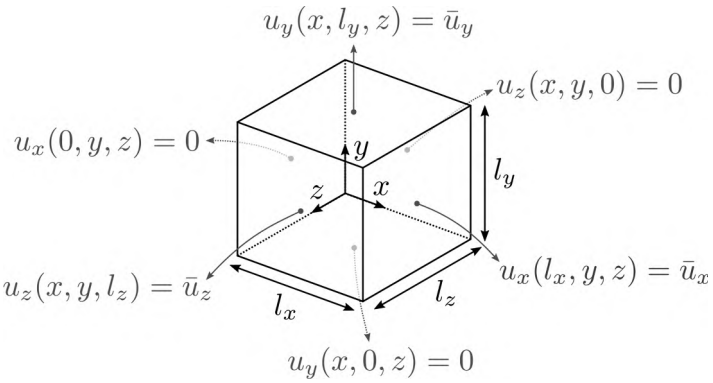

Fig. 4. Scheme of a cuboid, representative volume element with planar expansion boundary conditions.

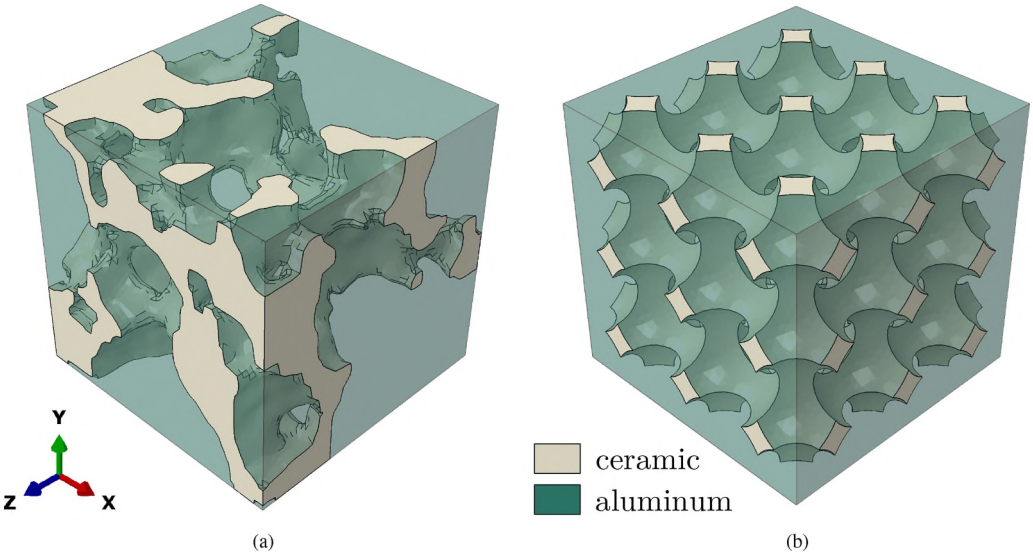

Fig. 5. Reconstructed (a) and simplified generated (b) microstructure of the IMCC with an Al_2O_3 fraction of 26 vol%.

Along the surfaces of the cuboid with the dimensions $l_x \times l_y \times l_z$ the displacement boundary conditions $u_i = 0$, $i \in \{x, y, z\}$ along the planes $x = 0, y = 0$ and $z = 0$ are used. The surfaces at $x = l_x, y = l_y$ and $z = l_z$ are enforced to stay planar, i.e. $u_i = \bar{u}_i$, during thermal extension to preserve the compatibility with adjacent RVE cells as shown in Fig. 4.

Thermal strains $\boldsymbol{\varepsilon}_{th}$ due to heating or cooling from a temperature T_1 to T_2 can be calculated by

$$\boldsymbol{\varepsilon}_{th} = \int_{T_1}^{T_2} \alpha_{th}(T)\, dT. \tag{4}$$

with the (temperature dependent) coefficient of thermal expansion $\alpha_{th}(T)$ of the respective material. Stresses are induced by thermal loading if a volume cannot expand freely. This can be caused by e.g. boundary condition constraints or in the case of the IMCC by neighboring materials with different expansion behavior. These stresses can be determined using

$$\boldsymbol{\sigma} = \mathbb{C}\,(\boldsymbol{\varepsilon} - \boldsymbol{\varepsilon}_{th}) \tag{5}$$

with the stiffness matrix $\mathbb{C}$ and the total strain $\boldsymbol{\varepsilon}$.

Linear elastic behavior is considered for the Al_2O_3 ceramic and an elasto-plastic model with J_2 plasticity and a rate independent Swift hardening law [31].

$$k = A\left(\bar{\boldsymbol{\varepsilon}}_{pl} - \boldsymbol{\varepsilon}_0\right)^n \tag{6}$$

Here, the equivalent plastic strain $\bar{\boldsymbol{\varepsilon}}_{pl}$ and the hardening parameters $\{A, \boldsymbol{\varepsilon}_0, n\}$ are used for the AlSi10Mg alloy. Isotropy is assumed for both materials. The hardening parameters $A = 442.67$, $\varepsilon_0 = 0.001$ and $n = 0.112$ at room temperature ($T = 25$) have been determined experi-

Table 1
Temperature dependent material input parameter for Al_2O_3 and AlSi10Mg. T is the temperature in $^\circ C$. It is used in a unitless form, i.e. $T{\cdot}K^{-1}$ in the presented equations. ΔT refers to the dimensionless difference $(T - T_t){\cdot}K^{-1}$ between the current temperature T and the transition temperature $T_t = 200\,^\circ C$ in the bilinear expression for the AlSi10Mg Poisson ratio. The parameters a –e for $\alpha_{th}(T)$ are given by: $a = 1.04{\cdot}10^{-5}$, $b = 1.88{\cdot}10^{-8}$, $c = -1.73{\cdot}10^{-11}$, $d = 1.66{\cdot}10^{-13}$ and $e = -3.68{\cdot}10^{-16}$. Regarding $\sigma_y(T)$, the corresponding parameters are: $f = 102.5$, $g = -100$, $h = -2.5$ and $j = 0.01$.

Material	Property		T-dependent value	
Al_2O_3	E	$[GPa]$	$351.31 - 5.25{\cdot}10^{-2}\,T$	[32]
	ν	$[-]$	$0.23 + 1.12{\cdot}10^{-5}\,T$	[32]
	α_{th}	$[K^{-1}]$	$6.24{\cdot}10^{-6} + 2.32{\cdot}10^{-9}\,T$	[32]
AlSi10Mg	E	$[GPa]$	$71.1 - 4.38{\cdot}10^{-2}\,T$	[4]
	ν	$[-]$	0.33 , for $T \leq 200\,^\circ C$ $0.33 + 1.4{\cdot}10^{-4}\,\Delta T$, else	[4]
	α_{th}	$[K^{-1}]$	$a + bT + cT^2 + dT^3 + eT^4$	Fig. 9
	σ_y	$[MPa]$	$f + g\tanh(h + jT)$	[33]

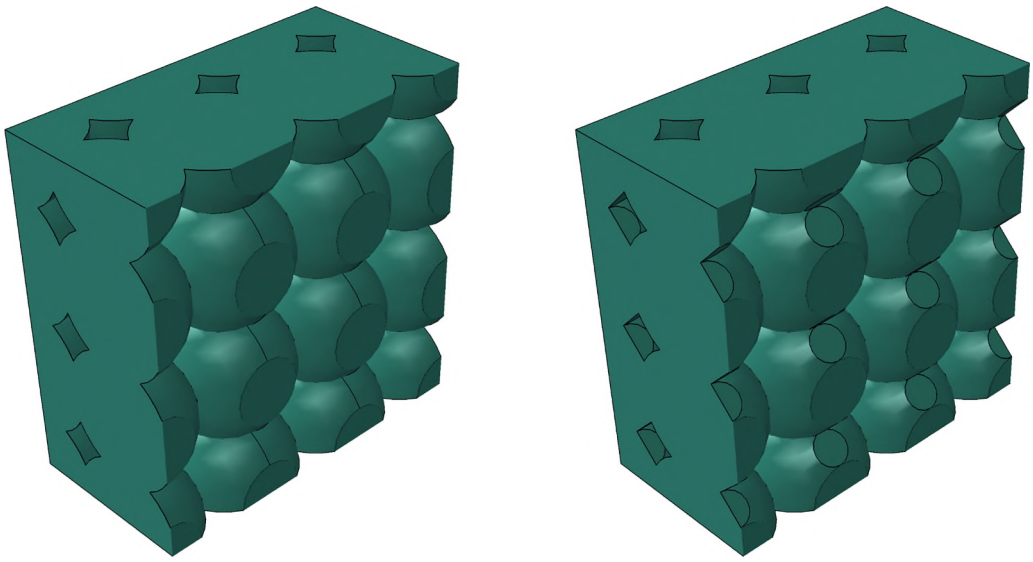

(a) (b)

Fig. 6. Cut view through the AlSi10Mg phase: (a) without pores and (b) with 1 vol.% pores included in the xy-plane of the AlSi10Mg.

mentally. Temperature dependent mechanical and thermal properties are implemented considering elastic constants ($E(T)$, $\nu(T)$) for both materials [4,32] and temperature dependent yield stresses $\sigma_y(T)$ for the AlSi10Mg [33] with parameters from literature.

As these material systems differ slightly from the ones in this study, the literature values have been fitted and scaled with respect to the experimental values for Al_2O_3 and AlSi10Mg determined at room temperature. For example, the hardening laws at the respective temperatures are derived by scaling the yield stress function k at room temperature with the ratio of yield strength at the respective temperature $k(T) = k(25°C)\,[\sigma_y(T)\,/\sigma_y(25°C)]$. Regarding the temperature dependent coefficient of thermal expansion $\alpha_{th}(T)$, values from literature [32] as well as the experimental results for the heating presented in Fig. 9 are applied to the numerical analyses for the Al_2O_3 and the AlSi10Mg, respectively. All relevant parameters and equations for the temperature dependent material properties are summarized in table 1.

4.2. Boundary condition and parameter variation

Parameter studies are performed to evaluate the influence of boundary conditions on the thermal expansion behavior and to correlate the results with different mechanisms described in literature [4,13,18,19].

Geometry

As already mentioned in Section 4.1, both reconstructed and generated microstructures are considered (cf. Fig. 5) to investigation whether geometrical simplifications of the microstructure are reasonable to achieve equivalent results with a reduced time consumption. The reconstructions are based on X-ray CT-scan images which have been segmented, binarized, filtered, smoothed and meshed according to Horny et al. [21,34]. For the generated structures, the metallic cavities are assumed to be spherical (see [34]), monodisperse and arranged in a perfectly ordered manner in order to study if anisotropic behavior is induced by certain boundary conditions.

Boundary conditions

The planar expansion boundary conditions at the volume element surface described in Section 4, cf. Fig. 4, are used in numerous numerical studies on the thermal expansion behavior [17,18,35–37] as they preserve RVE compatibility. However, a systematic comparison and influence of other boundary conditions is neglected in most investigations. In this study, two other models with (i) no expansion constraint and (ii) a constraint only at the surface in x-direction (replicating the experimental dilatometer setup) with $u_x = 0$ for $x = 0$ and $u_x = \overline{u}_x$ for $x = l_x$ are considered.

Pores

Idealized assumptions of a perfect infiltration are made in the basic model neglecting residual porosity in the aluminum phase. However, experimental [13] as well as numerical [18] investigations state that pores are relevant for the thermal strain hysteresis and lead to a general reduction of the CTE. As shown in Fig. 6, a model including pores in the AlSi10Mg directly at the interface is used to study these presumptions. Further, the pores are placed in a regular pattern only in the xy-plane to study anisotropy effects.

Interface

According to the literature, thermal strain hystereses found for interpenetrating metal ceramic composites can be explained by changing stress signs due to the load transfer between the two materials upon the heating/cooling change [4] as well as void formation, debonding and in-/extrusion of the metal phase at the surface [4,13]. These partially competing processes are studied using two extreme case scenarios considering the properties of the AlSi10Mg/Al_2O_3 interface. (i) A perfectly bonded interface between ceramic and metal is chosen to ensure a full load transfer and (ii) a free, frictionless contact constraint is used to allow for a relative motion of the materials caused by e.g. interface defects.

Initial cooling

As stated by Sharma et al. [19], thermal residual stresses due to initial cooling of the volume element, e.g. from the manufacturing process of the material, can not be neglected in a subsequent thermal expansion analysis. Therefore, we use varying initial cooling temperatures T_0 in a range of $200 - 600\,°C$ (cf. Fig. 3) and compare the results to microsturctures without initial cooling, thus starting from a stress free state at the first heating cycle.

Temperature dependent properties

In the basic model both thermal and mechanical parameters of AlSi10Mg were chosen to be temperature dependent. However, it is

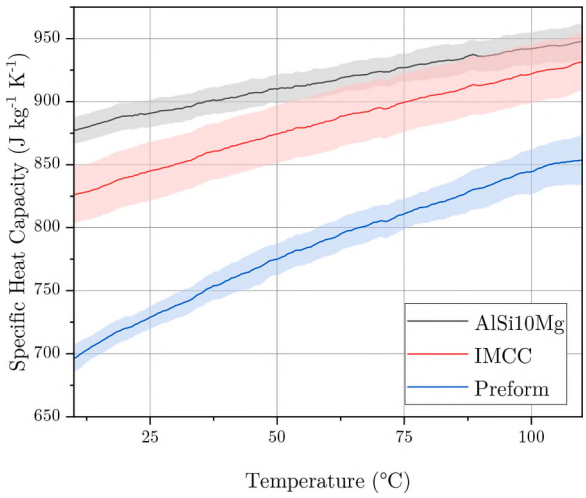

Fig. 7. Specific Heat Capacity of the aluminum alloy, IMCC and Preform.

uncertain whether the effective thermal expansion of the composite might also be a result of either T-dependent mechanical $E(T), \nu(T), \sigma_y(T)$ of both constituents combined with the interpenetrating microstructure. Both cases are studied in separate models.

4.3. Evaluation of modeling results

Unless mentioned otherwise, the CTE is determined in the first heating ($t_1 < t < t_2$) and cooling cycle ($t_2 < t < t_3$) presented in Fig. 3, respectively. For the calculation according to equation 3, the initial length of the VE in the respective direction $i \in \{x, y, z\}$ is chosen to be the length L of the sample at the time t_1, i.e. $L_{0,i} = L_i(t_1)$. Without an initial cooling, $L_{0,i}$ coincides with the initial cuboid dimension of the respective direction l_i (cf. Fig. 4). Upon thermal loading, the length change of the cuboid $dL(t)$ is determined by using the difference of the mean nodal surface displacements $\widehat{u}_i(t)$ in the respective direction in order to calculate the thermal strains $dL_i(t)/L_{0,i}$, with $dL_i(t) = L_i(t) - L_{0_i} = \widehat{u}_i$:

$$\widehat{u}_i(t) = \frac{1}{N_+}\sum_{n_+=1}^{N_+} u_{i,+}(n_+) - \frac{1}{N_-}\sum_{n_-=1}^{N_-} u_{i,-}(n_-), \quad i \in x, y, z \tag{7}$$

Here, $n_{+/-}$ denotes the current node and $N_{+/-}$ is the number of all nodes on the respective surface with the positive $(+)$ and negative $(-)$ normal vector. In the case of the basic model using planar surface constraints this can be simplified by tracking the displacements $\overline{u}_i$ directly, as $\widehat{u}_i(t) = \overline{u}_i(t)$ in this case.

The stress analysis of the single components Al_2O_3 and AlSi10Mg in a volume averaged fashion by integrating the volume weighted stresses over the volume V_c of the respective component c:

$$\langle \boldsymbol{\sigma} \rangle = \frac{1}{V_c}\int_{V_c} \boldsymbol{\sigma}\, dV\,. \tag{8}$$

For the stress evaluation we focus on the normal stress components $\langle \sigma \rangle_i$ in the respective directions $i \in \{x, y, z\}$. In general, the volume averaged stress tensor $\langle \boldsymbol{\sigma} \rangle$ is anisotropic, thus $\langle \sigma \rangle_x \neq \langle \sigma \rangle_y \neq \langle \sigma \rangle_z$. However, the simplified generated microstuctures and similar boundary conditions on every RVE surface result in an isotropic tensor. Therefore, in general only one value $\langle \sigma \rangle$ is displayed in the results and directional dependencies of the volume averaged stresses are mentioned explicitly.

Table 2
Thermal diffusivity a, specific heat capacity C_p and thermal conductivity λ of IMCC and alloy at room temperature and 100 °C.

Material	T [C]	a [$cm^2 s^{-1}$]	C_p [$J kg^{-1} K^{-1}$]	λ [$W m^{-1} K^{-1}$]
IMCC	20	0.317 ± 0.007	839	78
	100	0.343 ± 0.015	922	93
AlSi10Mg	20	0.539 ± 0.006	888	128
	100	0.573 ± 0.004	942	145

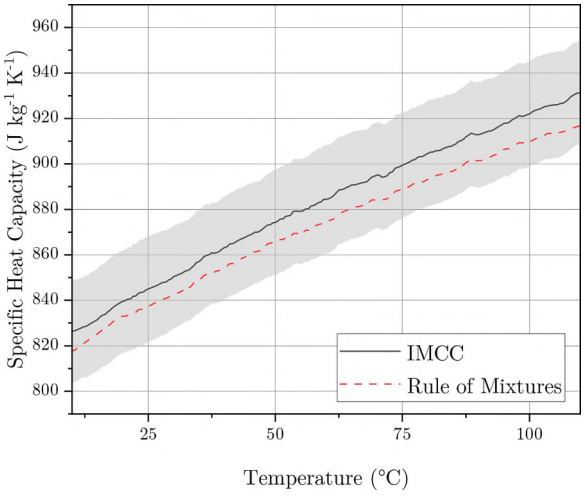

Fig. 8. Comparison of the specific heat capacity of the IMCC with the estimation from the rule of mixtures.

5. Results

5.1. Initial heating related experimental results

5.1.1. Specific heat capacity

The average specific heat capacity from the DSC measurements of six samples of the IMCC, among others, is shown in Fig. 7. The values increase from 826 $J kg^{-1} K^{-1}$ at 10 °C to a value of 931 $J kg^{-1} K^{-1}$ at 110 °C. The standard deviation over the complete temperature range is circa 50 $J kg^{-1} K^{-1}$.

For comparison, the specific heat capacities of alloy and preform are also shown. The former is clearly higher than that of IMCC at 20 °C. At higher temperatures, both materials reach similar values and the deviations overlap. The specific heat capacity of the ceramic foam is well below that of the IMCC but increases more steeply than the others. For preform and alloy, two samples each were measured. The standard deviation in both cases is much smaller than the IMCC's. The preform's deviation rises noticeably with increasing temperature. At room temperature, the specific heat capacity of the IMCC is 839 $J kg^{-1} K^{-1}$, that of the alloy is 888 $J kg^{-1} K^{-1}$, and that of the foam is 720 $J kg^{-1} K^{-1}$. Together with the values at 100 °C the values are noted in table 2 in Section 5.1.2.

In Fig. 8 the actual IMCC values are compared to calculated values obtained via the linear mixing rule of the two raw materials, which is shown in equation 9.

$$C_{p,c} = C_{p,m} \cdot c_m + C_{p,v} \cdot c_v \tag{9}$$

With $C_{p,c}$ being the composite's specific heat capacity and $C_{p,m}$ and $C_{p,v}$ being those of the matrix (AlSi10Mg) and the reinforcement (preform). c_m and c_v are the mass fractions of matrix and reinforcement. The calculated values for $C_{p,c}$ are somewhat lower, ranging from 816 $J kg^{-1} K^{-1}$ at 10 °C to 917 $J kg^{-1} K^{-1}$ at 110 °C. As the temperature increases, the deviation from the measured data increases slightly. The values according to the linear mixing rule are up to 1.5% lower than the

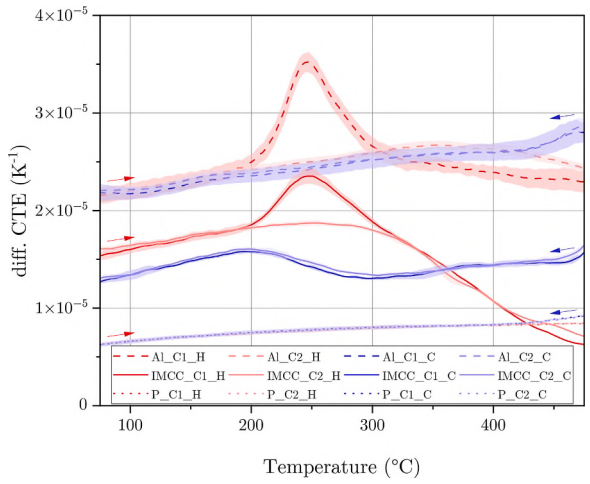

Fig. 9. Averaged coefficient of thermal expansion results for heating (red) and cooling (blue) of first (dark colour) and second (light colour) cycle for the AlSi10Mg alloy (dashed), the IMCC (straight) and the ceramic preform (dotted).

measured ones. To determine the fraction in weight percent, the values in volume percent were calculated with the densities of alloy and preform material. For AlSi10Mg, a density of $2670\,kg/m^3$ [38] results in a fraction of 66 *wt*%, and for Al_2O_3, with a density of $3950\,kg\ /m^3$ [39] gives a fraction of 34 *wt*%.

5.1.2. *Thermal diffusivity and thermal conductivity*

Values for thermal diffusivity and thermal conductivity are shown in table 2. Both characteristics increase with rising temperature. The thermal diffusivity of the IMCC increases by 8% when heated from 20 °C to 100 °C . Over the same temperature range, the diffusivity increase in the alloy is only 6%. Comparing the thermal diffusivity at room temperature, the value of the alloy is about twice that of the IMCC. The quality of the fit was very good in most cases. The largest deviations in the upper range occurred for the IMCC samples at room temperature. This is also reflected in the standard deviation of the thermal diffusivity. IMCC's thermal conductivity compared to the alloy is 61% at room temperature and 64% at 100 °C.

5.1.3. *Thermal expansion behavior*

The thermal behavior of the interpenetrating composite material and its components, the AlSi10Mg alloy and the alumina preform, are investigated and the results plotted in Fig. 9. As it is expected from manufacturing and described in literature [40], the internal stresses will be significantly reduced during the first heating cycle. Therefore, not only the first, but also the second cycle is plotted for all three materials and compared.

The ceramic preform has the lowest differential coefficient of thermal expansion (CTE) in a range between $6.3{\cdot}10^{-6}$ and $8.5{\cdot}10^{-6}\,K^{-1}$ (compare Schukraft et al. [25]). Heating and cooling curves are very narrow and within the standard deviation of the measurement identical to each other for both cycles. The aluminum alloy has the highest CTE, ranging between $2.16{\cdot}10^{-5}$ and $3.52{\cdot}10^{-5}\,K^{-1}$.

The AlSi10Mg alloy shows a peak-like increase of the CTE for the first cycle above 200 °C. This reaches its maximum approximately at 250 °C and decreases down to the level before the peak at around 300 °C. For higher temperatures, the curve ranges between $2.39{\cdot}10^{-5}$ (at 400 °C) and $2.29{\cdot}10^{-5}\,K^{-1}$ (at 500 °C). The second heating cycle of the AlSi10Mg alloy is much smoother and only ranges between $2.18{\cdot}10^{-5}$ and $2.66{\cdot}10^{-5}\,K^{-1}$. For higher temperatures it is above the curve of the first cycle. Except of the area around the maximum temperature, the cooling CTE curve of the aluminum alloy is very similar to the heating curve and runs slowly below the heating curve between 175 and 425 °C, but still within the standard deviation.

The IMCC has a CTE in the range of $7.3{\cdot}10^{-6}$ and $2.4{\cdot}10^{-5}\,K^{-1}$, with a significant peak-like increase in the first cycle, between 200 and 300 °C, with its peak at 250 °C. The second cycle has a slight increase from $1.4{\cdot}10^{-5}$ up to $1.8{\cdot}10^{-5}\,K^{-1}$. From 300 °C on, a strong decrease of the CTE sets in down to values below $1{\cdot}10^{-5}\,K^{-1}$, for the first and second cycle. The final value for the first cycle at 500 °Clies below the CTE of the ceramic preform. The cooling CTE of the IMCC is double the heating CTE at temperatures close to 500 °C and runs relatively horizontally, with a slightly negative slope (decreases from approximately $1.5{\cdot}10^{-5}$ (at 400 °C) to $1.3{\cdot}10^{-5}\,K^{-1}$ (at 300 °C). In the range from 300 °C down to 200 °C, an increase in the CTE is observable. From this local maximum, the value decreases down to $1.2{\cdot}10^{-5}\,K^{-1}$ for values below 100 °C.

In the following simulations, the input data to the numerical model is based on the second cycle.

5.1.4. *In-situ scanning electron Microscopy experiments*

For a closer investigation of microstructure related phenomena next to the dilatometry experiments regarding thermal expansion, in-situ experiments with a heating stage in a compression/tensile module were carried out in the vacuum chamber of an environmental scanning electron microscope. Images of the IMCC surface were captured at different magnifications and regions on the sample surface and at different temperature steps in a force-controlled experiment, so the linear encoder at the crosshead could be used to track the thermal expansion. For improved accuracy, detecting the sample expansion, digital image correlation was applied using the recorded images. For all SEM images, the facet pattern was applied and the optical strain was evaluated over the whole first heating and cooling cycle, with the strain values given for the surface analysis and an optical extensiometer. Fig. 10 shows the initial state of the mounted sample at room temperature and at 500 °C. Strain increases homogeneously with temperature over the whole heated area and the arithmetic average fits with the strain value of the optical extensiometer. At some heating steps, local

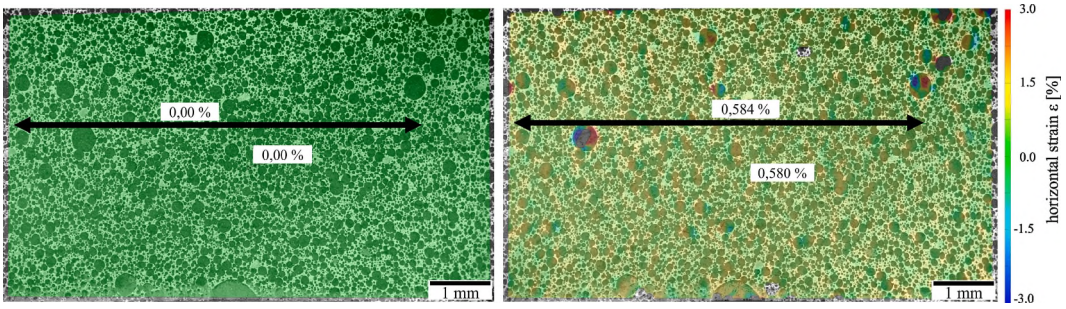

Fig. 10. Digital image correlation, based on the microstructural pattern of the composite surface during the first heating cycle at room temperature (left) and at 500 °C (right), with surface analysis (0.0 and 0.580% strain) and optical extensiometer (0.0 and 0.584% strain), represented by the black double-arrow. Strain scale is given on the right. At areas of bigger metal accumulations, the pattern cannot be identified correctly and results in miscalculated strain-bipoles.

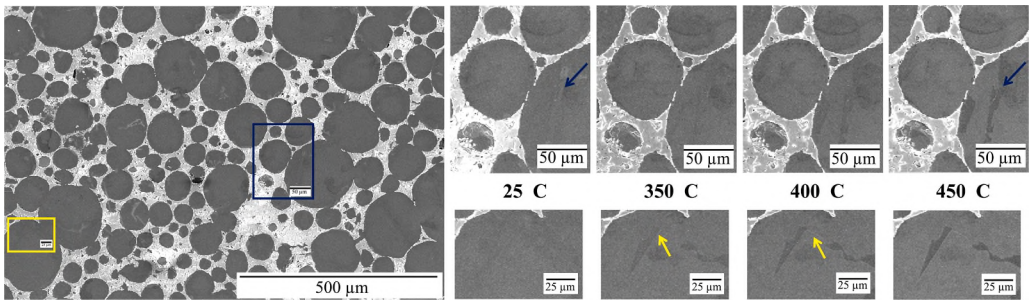

Fig. 11. Selected results with appropriate magnification from the in-situ SEM experiment. The two areas of interest are highligted in the overview image on the left and displayed for relevant temperature steps during the first in-situ heating cycle. In the upper row a pre-crack is highlighted with an arrow at room temperature and the compression of it displayed up to plastic compression of the fracture halves into each other (arrow on the right upper row). In the lower row a bigger metallic section is displayed, showing the formation of a crack at the phase boundary of the α-aluminum and a precipitation (arrow at 350 °C) and the crack growth into the α-aluminum phase (arrow at 400 °C). A scale bar is given for each image.

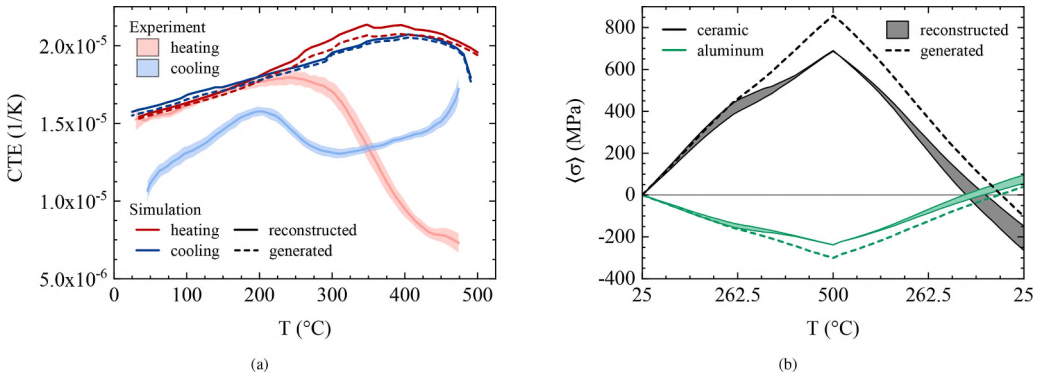

Fig. 12. Comparison of the thermal expansion behavior of reconstructed and generated microstructures without initial cooling: (a) CTE and (b) volume average stresses $\langle\sigma\rangle$. For the reconstructed microsturcture the mean CTE value and the $\langle\sigma\rangle$-range of x,y and z direction is shown.

facets could not be correlated with the initial step and form a gap on the strain surface. Bigger areas of the metal phase are difficult to be correlated due to their homogeneous gray scale and can therefore lead to miscalculation and the appearance of strain-bipoles, as they are visible for 500 °C on the right side of Fig. 10. At this maximum temperature of investigation, the strain on the surface reaches 0.580% for the surface analysis and 0.584% for the optical extensiometer.

CTE-Values of DIC evaluation are in the range from $6.5{\cdot}10^{-6}$ to $1.9{\cdot}10^{-5}\,K^{-1}$ and therefore within the range of dilatometry experiments, although they are not sensitive enough to fully represent the curve of the dilatometer. For the first cooling cycle, smaller steps were used between 300 and 175 °C (compare Fig. 2), to investigate the microstructural phenomena in the area of interest from dilatometry experiments, where an local increase of the differential CTE takes place. Neither in the DIC investigations, nor in the microstructural images a special hint for the explanation or any noticeable abnormality from the rest of the cooling section could be found.

For heating of the first cycle instead, a clear correlation between the dilatometry measurements and the microstructural changes could be found. Fig. 11 shows a representative SEM image on the left, with highlighted areas of interest and their local magnification on the right, for different temperature steps during the first in-situ heating cycle. As the blue arrow in the upper row highlights, a pre-crack is present within a metallic precipitation. For increasing the temperature, the crack seems to vanish, as the fracture halves are pressed together. For temperatures above 400 °C, major plastic deformation takes place and presses the fracture surfaces into each other. The lower row shows a bigger metallic area, where cracks are forming in the interface between a metallic precipitation and the α-aluminum at 350 °C and increasing to grow into the α-aluminum for higher temperatures (compare yellow arrow at 400 °C in the lower row of Fig. 11).

5.2. *Initial heating related simulation results*

5.2.1. *Geometry variation*

The thermal expansion behavior of both reconstructed and generated microstructures (cf. Fig. 5) have been modeled according to the basic model described in Section 4.1 without initial cooling (cf. Fig. 3). The numerical results of the T-dependent CTE and the volume averaged stresses during the heating-cooling-cycle are shown in Fig. 12. For both heating and cooling the results of reconstructed and generated microstructure are qualitatively similar as depicted in Fig. 12(a). All CTE curves exhibit an almost linear increase in the range of $25-250\,°C$, with a subsequent non-linear increase of the slope up to a peak value at approx. $T = 400\,°C$ and an eventual decline for $T > 400\,°C$. Quantitatively, the generated microstructure shows a slightly lower CTE for both heating and cooling. In case of heating the simulations yield values of $\mathrm{CTE}(25\,°C) = 1.54{\cdot}10^{-5}\,K^{-1}$, $\mathrm{CTE}_{max} = 2.13{\cdot}10^{-5}\,K^{-1}$ and $\mathrm{CTE}(500\,°C) = 1.96{\cdot}10^{-5}\,K^{-1}$ for the reconstructed compared to $\mathrm{CTE}(25\,°C) = 1.53{\cdot}10^{-5}\,K^{-1}$, $\mathrm{CTE}_{max} = 2.07{\cdot}10^{-5}\,K^{-1}$ and $\mathrm{CTE}(500\,°C) = 1.94{\cdot}10^{-5}\,K^{-1}$ for the generated microstructure.

Regarding the volume average stresses $\langle\sigma\rangle$ depicted in Fig. 12(b), an increase of tensile stresses in the ceramic and compressive stresses in the aluminum can be observed upon first heating from $T = 25\,°C$ to $T = 500\,°C$. In case of the reconstructed microstructures, the thermal expansion behavior is not perfectly isotropic, thus the range between maximum and minimum volume average stresses is displayed. The stresses of the Al_2O_3 and AlSi10Mg for both microstructure geometries coincide well up to a temperature of approx. 260 °C and the generated microstructure is the upper limit to reconstructed microstructures. For $T > 260\,°C$, the absolute value for both components increases stronger in the generated structures leading to $\langle\sigma\rangle_{Al_2O_3} = 857.9\,MPa$ and $\langle\sigma\rangle_{AlSi10Mg} = -300.2\,MPa$ at $T = 500\,°C$ compared to $\langle\sigma\rangle_{Al_2O_3} =$

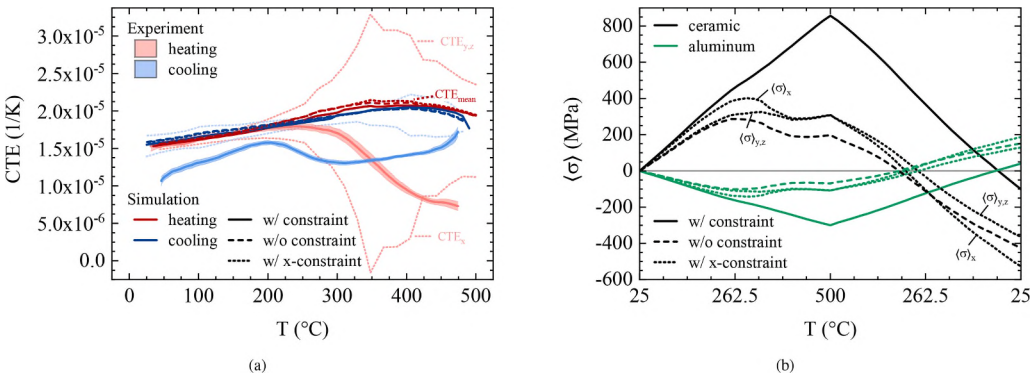

Fig. 13. Influence of different surface constraint boundary conditions on the thermal expansion behavior of generated microstructures without initial cooling: (a) CTE and (b) volume average stresses $\langle\sigma\rangle$. For the simulations using a planar surface extension constrain in x-direction only (dotted lines), the effective behavior of the IMCC is different in x- and y,z-direction. The CTE of the different directions CTE_x and $CTE_{y,z}$ as well as the mean value of all directions CTE_{mean} is given in (a). Same applies to the volume averaged stresses $\langle\sigma\rangle_x$ and $\langle\sigma\rangle_{y,z}$ in (b).

690.1 *MPa* and $\langle\sigma\rangle_{AlSi10Mg} = -273.9\,MPa$ in case of the reconstructed microstructure. Upon cooling, the tensile stresses in the ceramic and the compressive stresses in the aluminum are reduced and a change of sign is observed between $T = 167\,°C$ and 110 °C for the reconstructed and at approx. $T = 90\,°C$ for the generated microstructure. Back at $T = 25\,°C$, non-zero average stresses are observed for both components: $\langle\sigma\rangle_{Al_2O_3}$ from $-264.3\,MPa$ to $-148.4\,MPa$ and $\langle\sigma\rangle_{AlSi10Mg}$ from 55.5 *MPa* to 95.6 *MPa* for the reconstructed microstructure and $\langle\sigma\rangle_{Al_2O_3} = -100.8\,MPa$ as well as $\langle\sigma\rangle_{AlSi10Mg} = 40.1\,MPa$ for the generated microstructure.

5.2.2. Boundary condition variation

Generated microstructures (cf. Fig. 5) have been modeled according to the basic model (cf. Section 4.1) with modified boundary conditions as described in Section 4.2. The results of the first heating-cooling cycle without initial cooling using no planar surface constraints (*w/o constraint*) and a constraint only in x-direction (*w/ x-constraint*) are presented in Fig. 13 and compared to the basic model (*w/ constraint*) using constraints in all directions. The curves for the basic model (solid lines in Fig. 13) are already described in the previous Subsection 5.2.1 (dashed lines in Fig. 12).

In comparison, the model without constraints exhibits similar thermal expansion behavior for both heating and cooling as shown by the dashed lines in Fig. 13(a). The maximum heating expansion CTE = $2.11\cdot10^{-5}\,K^{-1}$ is 2.7% higher than for the fully constrained model and the peak is shifted to lower temperatures of approx. $T = 350\,°C$. Upon cooling, the maximum CTE difference between the basic model and the unconstrained model is 2.96% at $T = 25\,°C$. However, differences in the volume averaged stress can be observed as depicted in Fig. 13(b). Upon heating the extreme values occur at around $T = 270\,°C$ and they are reduced to $\langle\sigma\rangle_{Al_2O_3} = 286.6\,MPa$ and $\langle\sigma\rangle_{AlSi10Mg} = -101.0\,MPa$ for the ceramic and the aluminum, respectively. A subsequent decline of the absolute values is followed by an incline to $\langle\sigma\rangle_{Al_2O_3} = 197.6\,MPa$ and $\langle\sigma\rangle_{AlSi10Mg} = -68.7\,MPa$ at $T = 500\,°C$. Upon cooling, a stress free state in the IMCC is reached at $T = 330\,°C$ and the final stresses $\langle\sigma\rangle_{Al_2O_3} = -425.1\,MPa$ and $\langle\sigma\rangle_{AlSi10Mg} = 151.1\,MPa$ at $T = 25\,°C$ correspond to approx. four times the fully constrained model.

In case of the microstructures constrained only in x-direction, an anisotropic expansion behavior is observed. Especially upon heating, strong differences between the CTE in x- and in y,z-direction occur for temperatures > 200 °C as shown by the bright colored, dotted lines in Fig. 13. The CTE_x decreases down to $0\,K^{-1}$ whereas the $CTE_{y,z}$ increases up to $3.3\cdot10^{-5}\,K^{-1}$ at $T = 350\,°C$. At $T = 500\,°C$ the CTE ranges from $CTE_x = 1.12\cdot10^{-5}\,K^{-1}$ to $CTE_{y,z} = 2.36\cdot10^{-5}\,K^{-1}$. This anisotropy can be observed for the cooling as well, however in a less pronounced way. Averaging the CTE in all three directions results in the dark colored, dotted CTE_{mean} curves, which coincide very well with the basic model and the model without constraints. The peak upon heating at $T = 350\,°C$ is 4.2% higher than the value in the fully constrained model which represents the biggest difference between the curves. Upon cooling the values vary within ±2%. The volume average stresses (cf. Fig. 13(b), dotted line) are qualitatively equal to the model without constraints but they differ in x- and y,z-direction. Upon heating, the ceramic peak stress in x-direction $\langle\sigma\rangle_x = 400.9\,MPa$ is located at $T = 290\,°C$ whereas $\langle\sigma\rangle_{y,z} = 325.5\,MPa$ occurs at $T = 330\,°C$. After the local minimum of at $T = 405\,°C$, $\langle\sigma\rangle_x$ and $\langle\sigma\rangle_{y,z}$ of the ceramic coincide and reach 309.0 *MPa* at t_2. For the aluminum, the peak values of $\langle\sigma\rangle_x = -141.4\,MPa$ and $\langle\sigma\rangle_{y,z} = -114.5\,MPa$ increase to $\langle\sigma\rangle_{x,y,z} = -108.0\,MPa$ at $T = 500\,°C$. Upon cooling, a stress free state is reached between $T = 310\,°C$ and $T = 280\,°C$ for the x- and the y,z-direction, respectively. The final stresses at $T = 25\,°C$ range between $\langle\sigma\rangle_x = -526.7\,MPa$ and $\langle\sigma\rangle_{y,z} = -364.6\,MPa$ for the ceramic and $\langle\sigma\rangle_x = 186.6\,MPa$ and $\langle\sigma\rangle_{y,z} = 129.2\,MPa$ for the aluminum.

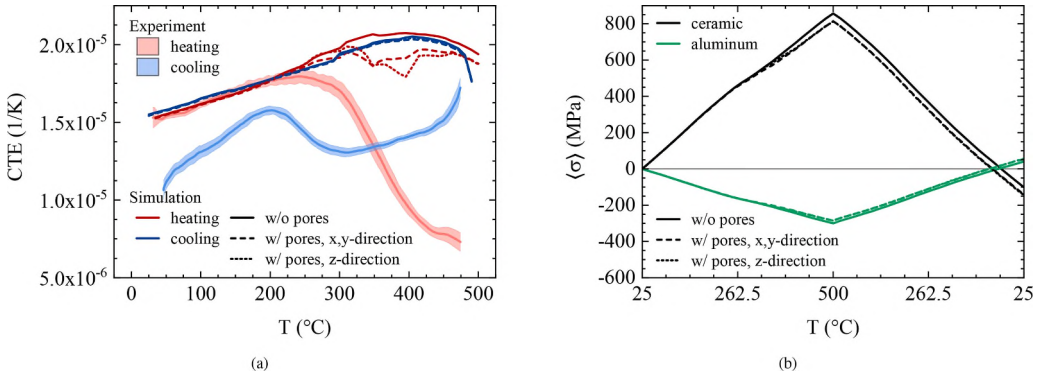

Fig. 14. Influence of pores on the thermal expansion behavior without initial cooling. Comparison to IMCC with pores: (a) CTE and (b) volume average stresses $\langle\sigma\rangle$. 1 *vol*% of pores are included in xy-planes of the aluminum phase at the interface.

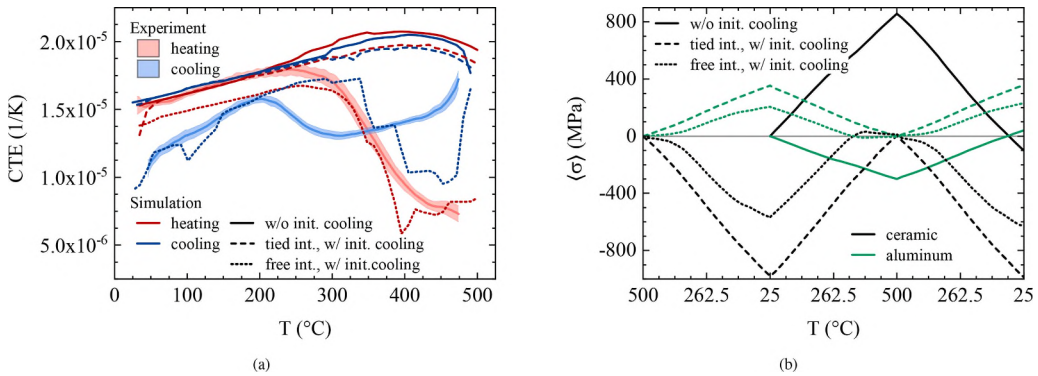

Fig. 15. Influence of interface properties on the thermal expansion behavior of generated microstructures with and without initial cooling from $T_0 = 500\,°C$: (a) CTE and (b) volume average stresses $\langle\sigma\rangle$ in x,y and z direction.

5.2.3. *Pore inclusion*

Generated microstructures (cf. Fig. 5) have been modeled according to the basic model (cf. Section 4.1) including 1 *vol*% of pores in xy-planes of the AlSi10Mg at the interface as shown in Fig. 6 in Section 4.2 without initial cooling. The results are presented in Fig. 14 and compared to the basic model without pores.

Including pores only in the xy-plane introduces an anisotropy to the IMCC behavior. Therefore, the xy-direction (dashed line) and the z-direction (dotted line) are examined separately. Compared to the microstructure without pores (solid line), the inclusion of pores shows no significant influence on the CTE behavior upon heating up to $T = 250\,°C$ as depicted in Fig. 14(a). For $T > 250\,°C$ the IMCC including pores exhibits a lower heating and curves between the directions differ upon further heating. Peak values of $1.97{\cdot}10^{-5}\,K^{-1}$ in xy-direction and $1.99{\cdot}10^{-5}\,K^{-1}$ in z-direction are observed. At $T > 450\,°C$ the heating CTE for all directions coincide again leading to a value of $\mathrm{CTE}(500\,°C) = 1.87{\cdot}10^{-5}\,K^{-1}$ at maximum temperature. In case of cooling, the microstructures with and without pores show similar CTE behavior.

Upon heating, the absolute volume average stresses in both components are reduced compared to the basic model without pores for $T > 250\,°C$ as shown in Fig. 14(b). As only very small differences of $< 0.1\%$ in the stresses between xy- an z-direction are observed, no distinction is made between the directions in the following description of the results. The maximum absolute stresses at $T = 500\,°C$ are $\langle\sigma\rangle_{Al_2O_3} = 813.6\,MPa$ and $\langle\sigma\rangle_{AlSi10Mg} = -285.5\,MPa$ for the ceramic and the aluminum, respectively. Upon cooling, the sign change occurs at a higher temperature of approx. 105 °C by incorporating pores compared to 90 °C in case of no pores. After final cooling at $t_3(T = 25\,°C)$, the volume average stress in the components are $\langle\sigma\rangle_{Al_2O_3} = -141.3\,MPa$ and $\langle\sigma\rangle_{AlSi10Mg} = 54.4\,MPa$.

5.2.4. *Interface variation*

Generated microstructures (cf. Fig. 5) have been modeled according to the basic model (cf. Section 4.1) with modified interface conditions as

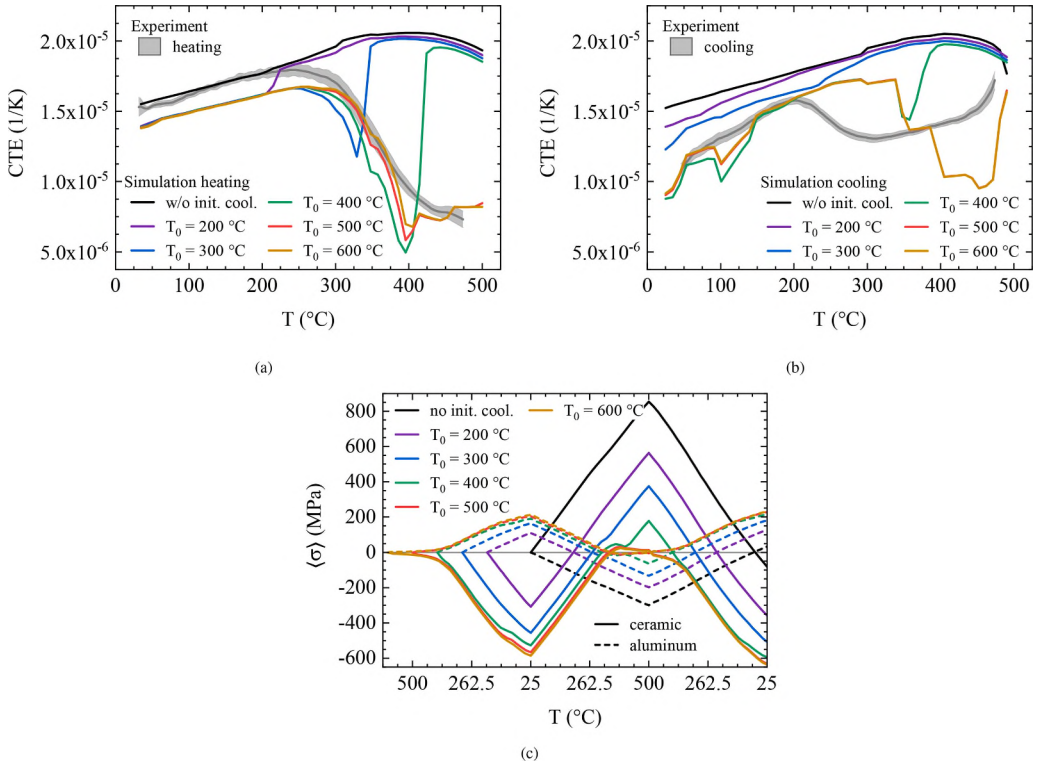

Fig. 16. Influence of different initial cooling temperatures $T_0 = 200 - 600\,°C$ on generated microstructures with free interfaces: (a) CTE at first heating, (b) CTE at first cooling and (c) volume average stresses $\langle\sigma\rangle$ in x,y and z direction.

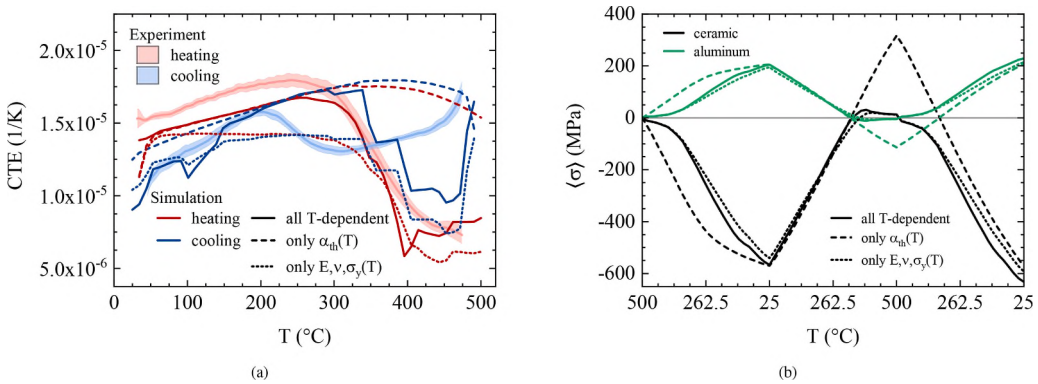

Fig. 17. Influence of T-independent mechanical and thermal properties on generated microstructures with free interfaces and initial cooling from $T_0 = 500\,^{\circ}$C: (a) CTE and (b) volume average stresses $\langle\sigma\rangle$ in x,y and z direction.

described in Section 4.2 both without and with initial cooling from $T_0 = 500\,^{\circ}$C. Without initial cooling, the results for the tied and the free interface coincide as shown in Fig. A.21 in the appendix. The results for microsturctures with initial cooling and tied (dashed line) as well as free interface (dotted line) are presented in Fig. 15 compared to the basic model without inital cooling (solid line).

Applying an initial cooling to a microstructure with a tied Al_2O_3/AlSi10 interface (dashed line) has no qualitative effect on the CTE compared to the basic model (solid line) as shown in Fig. 15(a). Including initial cooling reduced the CTE values upon both heating and cooling for temperatures $T > 300\,^{\circ}$C by an average of 5%. In Fig. 15(b) it can be seen that average compressive stresses of $\langle\sigma\rangle_{Al_2O_3} = -980.2\,MPa$ and tensile stresses of $\langle\sigma\rangle_{AlSi10Mg} = 353.5\,MPa$ are induced at t_1 ($T = 25\,^{\circ}C$, cf. Fig. 3) by initial cooling from $T_0 = 500\,^{\circ}$C in the ceramic and the aluminum, respectively. During heating, these thermal stresses are continuously reduced resulting in a sign change very close to $T = 500\,^{\circ}$C where $\langle\sigma\rangle_{Al_2O_3} = 2.26\,MPa$ and $\langle\sigma\rangle_{AlSi10Mg} = -0.92\,MPa$. Upon cooling, compressive stresses in the ceramic and tensile stresses in the aluminum build up again to $\langle\sigma\rangle_{Al_2O_3} = -989.0\,MPa$ and $\langle\sigma\rangle_{AlSi10Mg} = 357.7\,MPa$ at t_3.

For microstructures with a free interface (dotted line), an initial cooling from $T_0 = 500,^{\circ}$C has a remarkable effect on the T-dependence of the CTE, as depicted in Fig. 15(a). During heating, the initial CTE($T = 25\,^{\circ}C$) $= 1.38{\cdot}10^{-5}\,K^{-1}$ increases up to $1.68{\cdot}10^{-5}\,K^{-1}$ at $T = 260\,^{\circ}$C and subsequently decreases to reach a plateau level of $8.19{\cdot}10^{-6}\,K^{-1}$ at $T = 500\,^{\circ}$C. Further, a thermal strain hysteresis, i.e. a difference between heating and cooling CTE is observed, which represents the experimental findings in a qualitative manner. Regarding the stresses displayed in Fig. 15(b), lower absolute stresses due to the initial cooling $\langle\sigma\rangle_{Al_2O_3} = -567.2\,MPa$ and $\langle\sigma\rangle_{AlSi10Mg} = 205.3\,MPa$ compared to the tied interface are observed at t_1 for both components. Upon heating, a stress free state is reached at $T = 335\,^{\circ}$C. Subsequently, the tensile stresses in the ceramic and the compressive stresses in the aluminum increase slightly and reduce again to $\langle\sigma\rangle_{Al_2O_3} = 12.69\,MPa$ and $\langle\sigma\rangle_{AlSi10Mg} = -4.51\,MPa$ at $T = 500\,^{\circ}$C. Upon subsequent cooling, a change of sign regarding the stresses takes place immediately and on average, the stresses in the ceramic and the aluminum at t_3 are $\langle\sigma\rangle_{Al_2O_3} = -632.2\,MPa$ and $\langle\sigma\rangle_{AlSi10Mg} = 228.6\,MPa$.

5.2.5. *Initial cooling - T_0 variation*

Generated microstructures (cf. Fig. 5) have been modeled according to the basic model (cf. Section 4.1) with a modified free interface condition as described in Section 4.2 and varying initial cooling temperatures $T_0 = 200 - 600\,^{\circ}$C (see Fig. 3). The temperature dependent CTE upon heating and cooling as well as the volume averages stresses are shown in Fig. 16 in comparison to the a microstructure with free interfaces without initial cooling.

During heating the microstructures with a free interface subjected to initial cooling all CTE curves coincide for $T < T_0$ (see 16(a)) and follow the description of the microstructure with $T_0 = 500\,^{\circ}$C from Section 5.2.4 (dotted line in Fig. A.21). However, the IMCC exhibits a CTE jump up to the level of the microstructure without initial cooling when reaching the respective initial cooling temperature $T = T_0$. Only for $T_0 \geq 500\,^{\circ}$C the curves coincide and the CTE remains at a low plateau level for $T > 400\,^{\circ}$C. During cooling, the thermal expansion behavior differs from the heating for all initial cooling temperatures T_0 as presented in Fig. 16(b). Similar to the heating, the CTE curves follow the IMCC subjected to no initial cooling for $T > T_0$ and are slightly below it. At $T = T_0$ the curves clearly deviate downwards from the composite without initial cooling. For $T_0 > 500\,^{\circ}$C the cooling CTE differs completely from the microstructure without initial cooling revealing an increase followed by a decrease at $350\,^{\circ}C < T < 450\,^{\circ}C$ and a final increase of the CTE for $T > 450\,^{\circ}C$.

As shown in Fig. 16(c), the absolute volume average stresses in both components after initial cooling increase with T_0. In the ceramic stresses at $t_1(T = 25\,^{\circ}C)$ vary from $\langle\sigma\rangle = -308.4\,MPa$ to $\langle\sigma\rangle = -586.1\,MPa$. The volume average stress in the aluminum alloy varys between $\langle\sigma\rangle = 110.3\,MPa$ and $\langle\sigma\rangle = 212.9\,MPa$. Upon heating, the stress free state is reached between $T = 195\,^{\circ}$C for $T_0 = 200\,^{\circ}$C and $T = 350\,^{\circ}$C for $T_0 = 600\,^{\circ}$C. For initial cooling temperatures $T_0 \leq 400\,^{\circ}$C the maximum tensile stresses in the ceramic occur at $t_2(T = 500\,^{\circ}C)$, varying between $\langle\sigma\rangle = 563.1\,MPa$ for $T_0 = 200\,^{\circ}$C and $\langle\sigma\rangle = 178.6\,MPa$ for $T_0 = 400\,^{\circ}$C. This applies also to the compressive stresses in the aluminum ranging from $-198.2\,MPa$ to $-63.3\,MPa$. However, for $T_0 \geq 500\,^{\circ}$C the maximum stress in the Al_2O_3 of $\langle\sigma\rangle = 31.3\,MPa$ for $T_0 = 500\,^{\circ}$C and $\langle\sigma\rangle = 24.4\,MPa$ for $T_0 = 400\,^{\circ}$C located at $T = 385\,^{\circ}$C. Upon subsequent cooling, a on average stress free state occurs between $T = 225\,^{\circ}$C for $T_0 = 200\,^{\circ}$C and $T = 490\,^{\circ}$C for $T_0 = 600\,^{\circ}$C. At $t_3(T = 25\,^{\circ}C)$, stresses range from $\langle\sigma\rangle_{Al_2O_3} = -358.7\,MPa$ and $\langle\sigma\rangle_{AlSi10Mg} = 128.1\,MPa$ for $T_0 = 200\,^{\circ}$C and to $\langle\sigma\rangle_{Al_2O_3} = -637.6\,MPa$ and $\langle\sigma\rangle_{AlSi10Mg} = 231.3\,MPa$ for $T_0 = 600\,^{\circ}$C in the ceramic and the aluminum, respectively.

5.2.6. *Temperature dependent properties*

Generated microstructures (cf. Fig. 5) have been modeled according to the basic model (cf. Section 4.1) with a modified free interface condition, initial cooling from T_0 and T-independent mechanical or thermal material properties as described in Section 4.2. For the T-independent material properties the values at $T = 25\,^{\circ}$C are used, cf. table 1. The temperature dependent CTE upon heating and cooling as well as the volume average stresses are presented in Fig. 17 in comparison to the microstructure with free interfaces, initial cooling and T-dependent material properties.

As shown in Fig. 17(a) the heating CTE of the IMCC modeled with only temperature dependent expansion properties $\alpha_{th}(T)$ (dashed line), coincides with the curve of the model using all temperature dependent

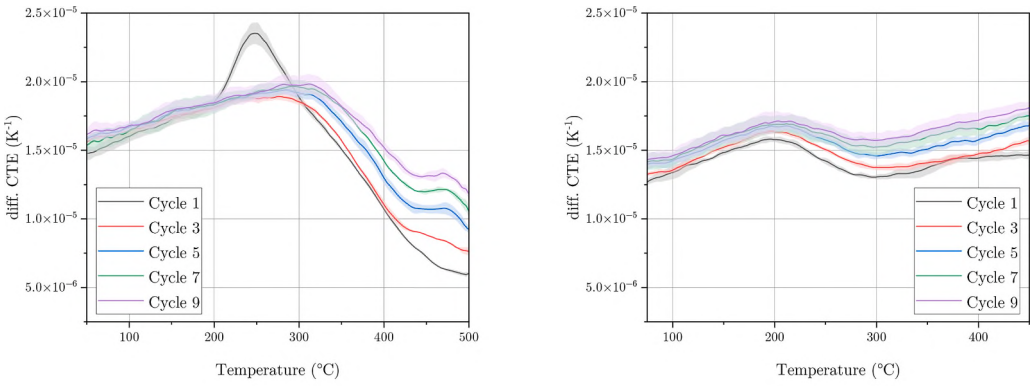

Fig. 18. Averaged CTE heating (a) and cooling (b) cycles 1-9 of three different samples.

parameters up to $T = 250\,°C$. Subsequently it increases further up to a maximum of $1.76{\cdot}10^{-5}\,K^{-1}$ and decreases again to $1.54{\cdot}10^{-5}\,K^{-1}$ at $T = 500\,°C$. The cooling CTE is similar to the heating CTE with $\leq 5.3\%$ higher values at high temperatures and $\leq 5.9\%$ lower values at low temperatures. Regarding Fig. 17(b)), the thermal residual stresses after initial cooling are equal to the model using all T-dependent parameters (solid line). Also, the stress free state upon heating occurs at the same location. However, using only T-dependent thermal properties results in maximum stresses at $T = 500\,°C$ of $\langle\sigma\rangle_{Al_2O_3} = 316.4\,MPa$ and $\langle\sigma\rangle_{AlSi10Mg} = -113.8\,MPa$ that differ significantly from the whole T-dependent curves. Upon cooling the sign change is at $T = 330\,°C$ and the final stresses at t_3 are $\langle\sigma\rangle_{Al_2O_3} = -571.5\,MPa$ and $\langle\sigma\rangle_{AlSi10Mg} = 207.3\,MPa$.

For the IMCCs modeled with only T-dependent mechanical properties $E, \nu, \sigma_y(T)$ (dotted line) the heating CTE is constant at $1.42{\cdot}10^{-5}\,K^{-1}$ for $T < 275\,°C$ as shown in Fig. 17(a). Then it reduces to $6.1{\cdot}10^{-5}\,K^{-1}$ for $T > 450\,°C$. The cooling CTE follows the curve of the all T-dependent parameter simulation in a qualitative manner with reduced absolute values. Also the volume averages stresses depicted in Fig. 17(b) show similar behavior to the all T-dependent simulations. Small differences can be observed in the stresses after initial cooling, the sign change upon heating and the remaining stresses after final cooling.

5.3. Cyclic heating related results

In addition to the first, respectively second heating cycle, the cyclic behavior and its influence on the microstructure and physical and mechanical properties was investigated and shall be presented in the following subchapter.

5.3.1. Cyclic thermal expansion and in-situ SEM experiments

In addition to the first two cycles, the dilatometry experiments were continued for seven more cycles and the heating and cooling cycles are presented for every second cycle with the average and standard deviation in Fig. 18 a) and b). As the diagram shows, the heating curves are very close for all nine cycles in the range up to 250 °C (except the first one with its already described peak at 250 °C). For temperatures above 300 °C, the curves continue in their linear CTE slope to higher temperatures with increasing cycle number and fall off less steeply. As the second cycle has its drop at around 300 °C and falls down to $7.3{\cdot}10^{-6}\,K^{-1}$, the ninth cycle has its drop at approx. 325 °C and only reaches values of $1.3{\cdot}10^{-5}\,K^{-1}$. The standard deviation decreases for all cycles from $3.88{\cdot}10^{-7}\,K^{-1}$ in average to $1.87{\cdot}10^{-7}\,K^{-1}$ in average. The cooling cycles show a similar behavior and an increasing CTE with increasing cycle numbers can be observed in the temperature range between 300 and 500 °C. For the ninth cycle, the local maximum at approx. 200 °C is almost not visible anymore in the cooling curve, as the CTE below 200 °C does only change slightly in comparison to the CTE above 300 °C.

Table 3
Maximum thermal strain values for cycle 1-4 at 500 °C measured with dilatometry for three different samples and with DIC on the in-situ SEM sample.

Cycle	In-situ SEM DIC [%]	Dilatometry [%]
1	0.580	0.72 ± 0.014
2	0.582	0.71 ± 0.013
3	0.608	0.72 ± 0.012
4	0.628	0.73 ± 0.006

Next to the CTE, the thermal strain is compared for the cyclic measurements between dilatometry experiments and DIC evaluation of the SEM images. In table 3 the values are compared for the first four cycles of the dilatometry experiments and the four measured cycles of the in-situ SEM evaluation.

For the microstructural evaluation, the cyclic testing results of the in-situ SEM experiments are presented in Fig. 19. The changes beyond the first cycle are in focus in this figure, but also significant changes during the first cycle, influencing the following cycles are highlighted within the figure and described below.

In the image Section 1 in Fig. 19 (first row), the influence of interfacial porosity is shown. The pore induced by manufacturing shows additional interface detachment during the first heating cycle, as highlighted with the arrow in the second column. For further thermal cycling, the detached area seems to stabilize and the pore does not grow anymore under heating, but narrows down (compare arrows in first row, column 5 and 6 in Fig. 19). For the cooling process, the pore expands in further cycling (cf. e.g. the arrows in first row, column 8 and 9 in Fig. 19). In image Section 2, the second row shows the development of interface detachment and its influence on intra-metallic porosity. In the first column, the arrow highlights intra-metallic porosity which shrinks strongly under increasing temperature in the first cycle (second column) and does not increase in the first cooling step anymore in favor interfacial detachment, formed in the upper area (cf. arrow in column 3). The interface detachment continues to enlarge over the four thermal cycles and finally covers a large part of the interface, as highlighted in the last column by arrows. In image Section 3, identical to the image section in Fig. 11 in the upper row, the influence of thermal cycling on the pre-crack in the metallic precipitation is presented and shows the crack closure at high temperatures (column 2, 4, 6 and 8) and increasing crack opening under cooling (compare column 3, 5, 7, and 9). In addition, in this section another, but very small interface detachment can be observed, closing at high temperatures and opening during cooling (analogous to image Section 1 in the first row). In image Section 4, the influence of thermal cycling on pre-cracks in precipitations and the α-aluminum is presented at the junction of two metal-filled spheres. An enlargement of the crack can be observed, as well as additional

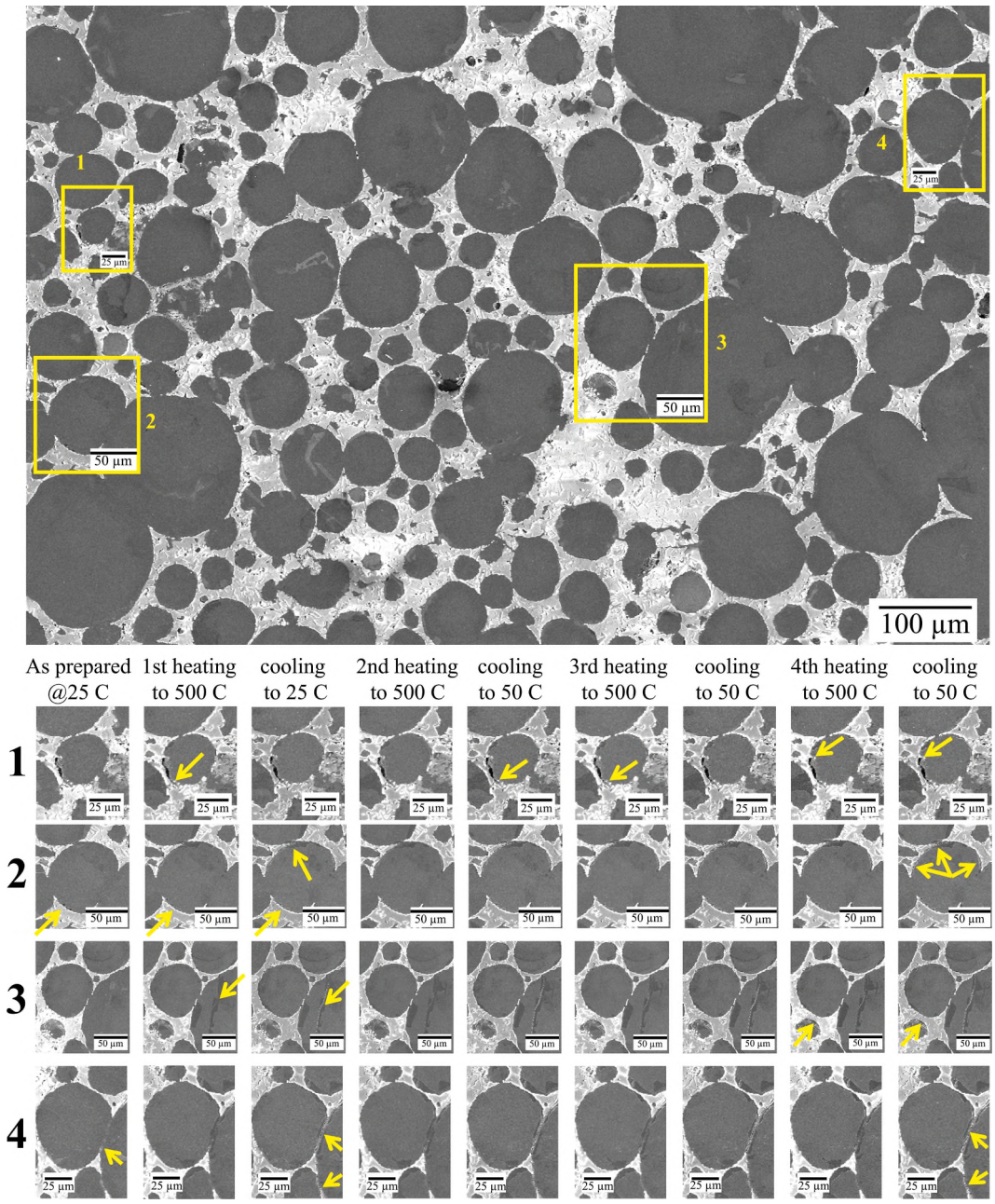

Fig. 19. Selected results with appropriate magnification from the in-situ SEM experiments under cyclic heating and cooling. The areas of interest are numbered and highlighted in the overview image on the left and displayed for the four temperature cycles (compare figure 2). Relevant changes are marked with arrows and described in the respective text.

detachment at neighboring interfaces between the α-aluminum and metallic precipitations.

5.3.2. Cyclic simulation of thermal expansion

Starting from the first cycle of the IMCC with free interfaces subjected to initial cooling from $T_0 = 500\,^{\circ}\mathrm{C}$ described in Section 5.2.5, additional 8 heating-cooling-cycles have been simulated. The results for the heating and cooling CTE over the temperature for the different cycles are shown in Fig. 20.

In the case of heating an increase of the CTE peak and a shift to higher temperatures can be observed with increasing cycle number, cf. Fig. 20(a). In the first cycle the peak of $1.68{\cdot}10^{-5}\,K^{-1}$ is at $T = 260\,^{\circ}\mathrm{C}$ whereas it increases to $1.77{\cdot}10^{-5}\,K^{-1}$ is at $T = 330\,^{\circ}\mathrm{C}$. The slopes of the subsequent CTE drop are very similar over the cycles and curves coincide at the same plateau level for $T = 500\,^{\circ}\mathrm{C}$. The cooling CTE curves displayed in Fig. 20(b) all show similar courses however the absolute CTE values increase slightly with the cycle number.

6. Discussion

6.1. Discussion of the experimental findings

In this section, the experimental findings are brought together, discussed and put into comparison to literature.

6.1.1. Specific heat capacity and thermal conductivity

The measurement of the specific heat capacity for the alloy is in good agreement with literature values (cf. CES EduPack database [38]. In comparison to the rule of mixture (cf. Fig. 7), the composite has an identical curve in the range of standard deviation and shows that the

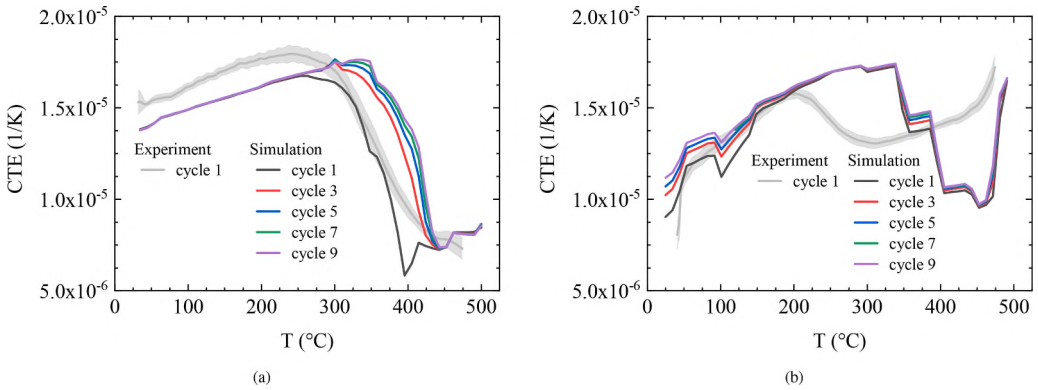

Fig. 20. Influence of thermal cycling on the thermal expansion behavior of generated microstructures: (a) heating and (b) cooling CTE of thermal cycles 1-9 with initial cooling from $T_0 = 500\,^{\circ}\mathrm{C}$.

interpenetrating microstructure does not influence the heat capacity.

The thermal conductivity of the composite underlies bigger reduction by the ceramic phase, than the specific heat capacity and has a comparable value to iron at room temperature [41]. Reasons for that can be found in the microstructure of the spherical shaped metallic parts, which are only connected at a small cross-section with each other. Another reason is the porosity and damage due to manufacturing, as cracks in the metalic phase (c.f. Fig. 11. This reduces the thermal conductivity for 20°Cin comparison to the aluminum alloy about 39 %. For increasing temperature, the higher thermal expansion and further phenomena, discussed in detail in Section 6.1.2, lower the reduction in thermal conductivity and at 100 °C, the thermal conductivity of the composite is only reduced by 36 % in comparison to the aluminum alloy. This is an increase of 3 % in comparison to 20 °C. For higher temperatures, an increasing improvement of thermal conductivity is expected, as porosity lowers and interface detachments are closed due to the expanding metallic phase (cf. Fig. 19.

6.1.2. Dilatometry and in-situ SEM investigations

As the results in Fig. 9 show, the ceramic preform has the lowest CTE with an almost linear behavior and identical behavior for heating and cooling in the investigated temperature range. The AlSi10Mg alloy instead shows a strong difference between the first and second heating cycle between 200 and 300 °C. This allows the conclusion that the influence of the peak in the IMCCs CTE curve is affected by the metallic phase. Other authors investigating metal-ceramic composites or even interpenetrating composites, only evaluated the strain-temperature diagram (Balch et al. [17]), investigated systems with pure aluminum (Skirl et al. [13]) without this phenomenon or did not take the CTE values of the first cycle into account (Roy et al. [16]). Huber et al. [4] investigated two composites with pure aluminum as well as an aluminum alloy (AlSi7Mg), measured a peakless first CTE curve for the pure aluminum and detected the same peak for the AlSi7Mg alloy. They also refer on studies, where AlSi7 without magnesium was investigated and stated, the low ratio of magnesium (0.5%) does not have an influence on the peak, as it also appeared for AlSi7 [42]. They followed in their discussion, the phenomenon originates in the T4 treatment of the AlSi7(Mg) alloy and the slow heating rate of $5\,K/min$ brings the quenched and supersaturated Si in a thermodynamic equilibrated solution and causes the peak [43]. They state for further cycles that the heating and cooling rate is too low to generate supersaturation and therefore, the peak does not appear anymore. In our investigated material system with the AlSi10Mg alloy, the cooling rate during manufacturing is in the range or below the $5\,K/min$ (compare chapter 2), which should result in the peak not being observed in the first cycle. Nevertheless, we also observe a peak in the first cycle for our material system and therefore we state the following explanation for that phenomenon:

After the infiltration of the ceramic preform with the AlSi10Mg alloy, individual samples were cut from the composite material, which has cooled down in the infiltration process throughout. The same was done for the AlSi10Mg alloy, which had been also subjected to infiltration in order to examine the microstructure identical to the one of the alloy in the composite. In the cooling process of the liquid alloy, various precipitates develop as a result of solidification up to the eutectic temperature (compare Mrvar et al. [22] in Voncina et al. [23]). These form a ”composite” in the metallic phase of different CTEs, Young’s modulus and yield and tensile strength - for the AlSi10Mg alloy in the same way, as for the AlSi7 and AlSi7Mg alloy. Residual stresses occur in this process (compare Sharma et al. [19], Agrawal et al. [44] and Hoffman et al. [14]), and lead in the cut samples to an uneven internal stress distribution. For reasons of homogenisation with the driving force to reduce mechanical energy in form of distortion energy, residual stresses are reduced in the composite from an activation temperature of 200 °C, and the aluminum alloy in the first cycle and lead to an temporary increase in CTE. The pure aluminum on the other hand does not form any precipitation and therefore has no peak-like behavior in the first heating cycle, as it is observed by Skirl et al. [13] and Huber et al. [4] for the composite with pure aluminum. In the conclusion of this argumentation it can also be stated that the activation temperature for inner processes in the metal phase (of the composite) is in the range of 200 °C, as Fig. 9 shows with the onset of internal activities.

For the following course of the CTE curve, Huber et al. [4] state the re-dissolution of up to 0.8% Si in the α-aluminum as a reason for the CTE decrease from 300 °C on, as the atomic volume decreases due to the substitutional Si in the Al lattice. This decrease is visible for the first cycle of the AlSi10Mg samples, for the second cycle from about 360 °C and for the composite in the first cycles from 300 °C, for the further cycling it is shifted to higher temperatures. The solubility of Si in the α-aluminum is for sure one of several processes taking place at elevated temperatures within the composite, but next to this other and more dominant processes are taking place, like changes in residual stress and porosity, creep, plastic deformation and crack formation, as well as interface detachment. Fig. 11 has shown the closure of pre-cracks, formed in precipitations in the metal phase during manufacturing (compare Morbitzer et al. [45]). This is a result of increasing residual stress in the metallic phase during heating. The onset of visible crack formation at 350 °C in the composite shows, damage is another phenomena going beyond the plastic deformation at elevated temperatures. Besides, the material throw-up from the compressed crack halves at 450 °C in Fig. 11, and accompanied creep (compare [46]) shows the reduced influence of the metallic phase and the increasing dominance of the ceramic phase in this temperature range. The CTE of the IMCC finally reaches values below the ceramic preform, which was already explained by some of the authors in Schukraft et al. [25] and results from the high porosity content of the ceramic preform (74%), because the

porosity allows higher transverse strain than a bulk material (bulk alumina [14] or the IMCC). The second cycle of the aluminum curve differs from literature values, presented by Jiang, et al. [47]. Better agreement of the data is found with Gumbleton et al. [48] for the range up to 177 °C.

In comparison to the experimental data, analytical models of CTE prediction should be discussed: The rule of mixtures only takes the volume fraction and individual properties of the two materials into account and therefore does not consider microstructural reasons or interaction, as the interfaces have to be slide free and the constituents flow free. Other models, set up from Turner [49], Kerner [50] or Scharpery [51] take this, at least partly, into account. Turner considers a strong interface and homogeneous strain within the composite, Kerner a strong interface for an enclosed sphere in another with elastically deforming phases. Scharpery extended the models to linear visco-elastic materials [52] and later extended his model to range within an upper and lower bound for volumetric and linear thermal expansion, based on energy principles [51], and discussed the extend to non-linear materials [53]. Huber et al. find good correlation with the Turner model up to 200 °C for heating of their composite, but due to plastic deformation, there is no valid correlation at higher temperatures anymore. This strengthens the conclusion, made from the peak-like behavior of the first cycle of thermal heating, that non-linear processes in the metal phase are activated above this temperature. Hoffman [14] and Skirl [13] make the more complex microstructure, the time depencence due to high residual stresses and the uneven behavior of the linear elastic ceramic and the visco-plastic metal responsible for the mismatch between the analytical models and their results. The deviation of the here investigated material system from the models is even higher due to the lower ceramic content in the IMCC and confirm the argumentation in literature with our investigations.

Furthermore, the DIC evaluation will be discussed in this chapter. In the surface strain calculation, bi-poles formed locally, as it is visible in Fig. 10 on the right side. The GOM-Correlate software needs neighboring facets to calculate the strain of the observed facet. If neighboring facets are missing due to the lack of contrast in metallic areas, strain bi-poles can be formed. This anomaly only appears locally and in individual frames and mostly disappear directly again in the next frame. Therefore, these are not a material phenomena. As the comparison of the strain values of the surface analysis and the optical extensiometer show, the bi-poles almost eliminate each other and do not influence the average value in a strong way. The influence of the sensitivity of the first derivative (differential coefficient of thermal expansion) instead deviates from the CTE curve, measured in the dilatometry experiment. Combined with the uncertainty of temperature at the investigated sample surface during the in-situ SEM experiments, the final results of the DIC show that the CTE cannot be measured as sensitive as in the dilatometry setup. Nevertheless, to the best of the authors knowledge, this is the first time in literature that the CTE was captured and evaluated on the sample surface within an in-situ SEM experiment for interpenetrating phase composites. Possible improvements could be achieved with a trained AI-algorithm and DIC-software, especially developed for SEM or microscopy gray-scale images.

6.2. *Discussion of the numerical findings*

As shown in Fig. 12 in Section 5.2.1, the CTE and the internal stresses of reconstructed and generated microstructures are in good agreement. Especially the CTE curves match very well and are in good agreement with the heating experiments for $T < 250\,^{\circ}\mathrm{C}$. The internal stresses in the generated structure exceeds the stress in the reconstructed IMCC. An explanation for the lower CTE and the increased stresses is the regular geometry of the generated structures with relatively thick ceramic rods in all directions and sharp edges. These prevent an unhindered expansion of the AlSi10Mg phase and lead to local stress concentrations at the sharp edges. Nonetheless, the deviations due to the geometry simplification are acceptable regarding the reduced computation time of the generated microstructures. Therefore, only generated microstructures are used in the other numerical investigations.

As presented in Fig. 13 in Section 5.2.2, a planar expansion constraint in all directions and no constraint in any direction yields almost identical results for the CTE over temperature. Applying a planar surface constraint in x-direction only, results in strong anisotropies regarding the CTE parallel and perpendicular to this direction. Averaging over all directions, the resulting curve coincides with the other two boundary condition approaches. However, using anisotropic boundary conditions and evaluating the expansion only in one direction leads to physically not reasonable CTE values. The small differences in the (mean) CTE curves of the different boundary conditions can be explained by the thermal strain calculation shown in equation 7 which is based on the mean displacement of the respective surface nodes. Using unconstrained surfaces, this can lead to deviations and may not be an ideal measure. As expected, the volume average stresses are reduced with less surface constraints at the boundaries. Overall, the plausibility of the planar expansion boundary conditions proposed in literature [17,18,35–37] can be confirmed in this study and has been used in all of the other simulations.

Incorporating pores in the aluminum leads to a reduction in the heating CTE for $T > 250\,^{\circ}\mathrm{C}$ as shown in Fig. 14. This is in accordance with the experimental results discussed in Section 6.1.2 and the simulations of Shen [18]. It has to be stated, that in [18] a much higher pore fraction of 7% is used and the thermal strain hysteresis is mainly effected if pores occur in a composite with a non-continuous aluminum phase. In this study, with a pore fraction of 1% the effect is far less pronounced. Further, the interpenetrating microstructure imposes less expansion constraints to the metal phase, which reduces the impact of pores in accordance to the findings of a composite with a continuous aluminum phase in [18]. Unlike in literature, the thermal strain hysteresis and the CTE difference between heating and cooling does not occur over the whole temperature range of the thermal cycling. Therefore, this study suggests that a reasonably small fraction of residual porosity or pores in the metallic phase due to imperfect infiltration is not solely responsible for the temperature dependent CTE behavior and the big differences between heating and cooling behavior.

Varying the interface properties has little to no influence on the CTE and the internal stresses during the first heating and cooling if no initial cooling is applied as shown in Fig. A.21 in the appendix. However, if an initial cooling is included, the interface properties have a major influence on both quantities as presented in Section 5.2.4, Fig. 15. The CTE drop at $T = 300\,^{\circ}\mathrm{C}$ in the heating experiments can only be observed in the numerical model by using free interfaces and initial cooling. This also accounts for the thermal strain hysteresis resulting in different CTE behavior for heating and cooling. Especially for the heating, free interfaces and initial cooling lead to an underestimation of the CTE for $T < 300\,^{\circ}\mathrm{C}$ as a detachment of the two components at large areas of the interface for the used initial cooling temperature $T_0 = 500\,^{\circ}\mathrm{C}$. For $T > 300\,^{\circ}\mathrm{C}$ the simulation result matches very well with the experimental findings, indicating that the relative motion of the Al_2O_3 and the AlSi10Mg at the interface becomes relevant at higher temperatures. Remaining differences between the CTE curves for heating and cooling might result from the oversimplified interface conditions as well as missing implementation of high temperature induced mechanisms like creep and damage. Further, a relation between internal stresses and the CTE response can be determined, as the major CTE drops are always accompanied by sign changes of the average stress in the components. Huber's [4] explanation for the thermal strain hysteresis due to changing stress signs upon heating/cooling change can also be confirmed by the numerical model.

The variation of the initial cooling temperature in Section 5.2.5 confirms these findings. As depicted in Fig. 16, every jump or drop of the CTE is accompanied by a sign change or a significant slope change of the stress curve. This is in accordance with [19], stating that thermal

residual stress is not negligible in a thermal expansion analysis. Regarding the heating, it can be observed that the CTE curves of $T_0 = 500\,^{\circ}\mathrm{C}$ and $T_0 = 600\,^{\circ}\mathrm{C}$ coincide at what is referred to as the "lower level" in the following. For initial cooling temperatures $< 500\,^{\circ}\mathrm{C}$ a jump from this lower level up to the upper level represented by the CTE curve of the IMCC without initial cooling can be noticed. Similarly, a deviation from the upper level at the initial cooling temperature for $T_0 < 500\,^{\circ}\mathrm{C}$ occurs upon cooling.

As shown in Fig. 17 in Section 5.2.6, both the temperature dependent thermal $\alpha_{th}(T)$ and mechanical $E(T), \nu(T), \varepsilon_{pl}(T)$ properties have an influence on CTE and internal stresses. However, different temperature ranges can be determined in which the dominance of the respective parameters varies. Upon heating, temperature dependent thermal properties are sufficient to describe the CTE behavior for $T < 250\,^{\circ}\mathrm{C}$. In this low temperature range also the volume average stresses are represented correctly. For high temperatures $> 350\,^{\circ}\mathrm{C}$, T-dependent mechanical properties are relevant to describe the CTE decrease and the internal stresses correctly. In case of cooling, $E(T)$, ν(T), $\varepsilon_{pl}(T)$ are dominant for the slope of the CTE curve, however using only temperature dependent mechanical properties results in a poor quantitative agreement with the all T-dependent simulations. With this knowledge, the conclusions often drawn in the literature that discrepancies between numerical models and experimental investigations might result from not using temperature dependent mechanical properties of the metallic phase (e.g. yield stresses) [19] can only be partly confirmed. This holds true for a high temperature regime whereas for low temperatures, using temperature dependent coefficients of thermal expansion $\alpha_{th}(T)$ for both constituents is sufficient.

6.3. *Discussion of the findings from thermal cycling*

In this sub-chapter, the findings from experimental and numerical investigation are combined.

Cyclic heating influences the microstructure of the composite, as described for Fig. 19, and the microstructural phenomena have an influence on the CTE behavior. In the following, the complex interaction of the phenomena should be put in context and compared to findings published in literature. Residual porosity in the composite was investigated and pores are influenced by internal stresses and change their size. Balch et al. state that the compression of porosities at elevated temperatures comes from the higher thermal expansion of the metal phase [17]. In the here investigated composite, this is observed in the experiments for increasing cycle number. For the first cycle instead, the in-situ experiments showed, that residual porosities are growing under heating. Under cooling, the pores should grow regarding Balch et al., and also this finding can be confirmed for higher cycle numbers in our investigations. In the first cycle however, intra-metallic porosity is reduced during cooling, in favor of interfacial debonding (cf. Fig. 19).

In the cyclic heating CTE curve, there are no markable changes up to $250\,^{\circ}\mathrm{C}$. The drop in the CTE curve increases with cycle number and is suggested to be associated with increasing solidification. With increasing cycle number also the interfacial detachment and plastic deformation and therefore, internal stresses relaxation took place over the cycles. This lessens the decrease of the CTE, induced by pore closing of the metallic phase, as stated by Huber et al. [4]. The numerical modelling shows this effect clearly in good agreement with the experiments and gives deeper understanding of the temperature dependency of the mechanical properties and their dominance for temperatures above $300\,^{\circ}\mathrm{C}$, as well as the role of interface detachment for modelling the effects, observed experimentally.

In case of cyclic cooling, the CTE behavior cannot be fully explained by this study, however important insight and indicators of possible explanations could be gained. Both experimental (cf. Fig. 9) and numerical (cf. Fig. 16) findings reveal a CTE jump upon the heating-cooling change at $T = 500\,^{\circ}\mathrm{C}$. This jump is a result of a sign change in the internal stresses as shown by the simulative analysis, which is in accordance to the assumptions of Huber et al. [4]. With successive temperature decrease during cooling, the experimental CTE curves decrease to a local minimum at approx. $300\,^{\circ}\mathrm{C}$ and subsequently increase to a local peak at $T = 200\,^{\circ}\mathrm{C}$. In the numerical investigation we have seen, that at high temperatures in particular, the temperature dependent mechanical properties of the AlSi10Mg are decisive for the CTE's behavior. Therefore, the continuing solidification of the AlSi10Mg and the increase of its mechanical stability for temperatures below $300\,^{\circ}\mathrm{C}$ could be the reason. Still active mechanisms, like dislocation creep and under internal stresses also further creep mechanisms (compare Ashby et al. [46]), counteract the CTE increase and the resulting dominance of the aluminum alloy partly. From temperatures in the range of $200\,^{\circ}\mathrm{C}$, thermally activated processes come to a standstill and the increase in dominance of the metallic phase reaches its maximum in the CTE curve. Rising internal stresses, due to the lack of compensation by creep, result in damage and interface detachments, which reduces the stress transfer between the AlSi10Mg and the Al_2O_3.

This assumption is supported by the fact that the simulations using a free interface between the two components coincide very well with the experiments for temperatures below $200\,^{\circ}\mathrm{C}$. Differences between simulation and experiment, especially in the high temperature regime, might result from the fact that no mechanisms like creep and damage have been considered in the numerical approach.

During thermal cycling, the CTE curves shift upwards with increasing cycle number as shown in Fig. 18. This might be due to the cyclic hardening of the AlSi10Mg over the number of cycles leading to an increased load transfer between the components. Further, the local peak at approx. $200\,^{\circ}\mathrm{C}$ shifts to higher temperatures with increasing cycle number. We assume, that due to the increasing plastification of the aluminum alloy over the cycle number, the point of sign change for internal stresses shifts to higher temperatures upon cooling which leads to the shift of the peak. The thermal cycling simulation presented in Section 5.3.2, Fig. 20 is capable of describing the evolution of cooling CTE over the cycle number and it can also reproduce the trends and tendencies from the experimental findings shown in Fig. 18 in a qualitative manner. Again, differences, especially in the high temperature regime might result from the fact that no mechanisms like creep and damage have been considered in the numerical approach.

7. Conclusion

The experimental approach combining dilatometry and in-situ SEM with DIC imaging, shows great potential for the investigation of the macroscopic thermal expansion behavior with a direct link to the microstructural evolution of the material system. Combined with numerical investigations, the following mechanisms could be determined:

- microstructural changes during heating and cooling in form of crack formation occur in the metallic phase and metallic precipitation.
- porosity has an influence on the CTE behavior of the composite, but no decisive in the range of the porosity present in the composite investigated.

Further conclusions could be drawn on the effect of the temperature dependent CTE upon heating:

- contrary to previous research, the peak in the CTE curve during the first heating cycle of the IMCC arises from the thermal activation of the internal stress relaxation in the metallic phase and its precipitates.
- interface detachment and changes of pore size emerge during cyclic heating.
- phenomenon explanation of the peak in the CTE curve during first experimental heating cycle due to residual stresses and damage was determined.

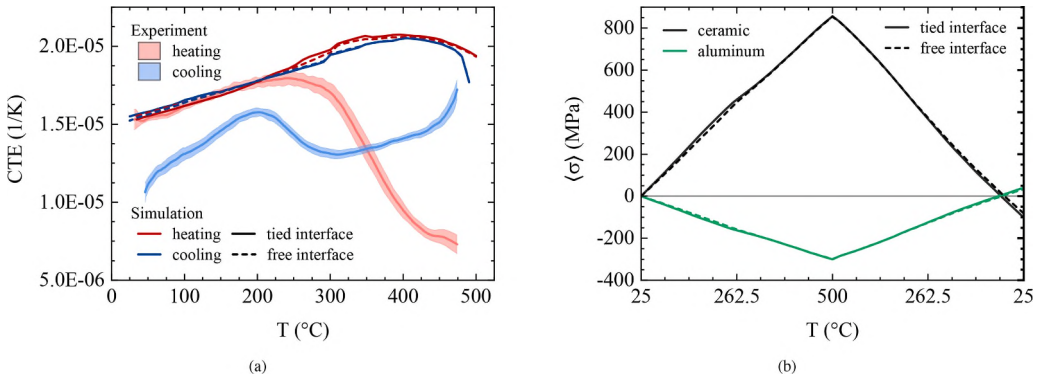

Fig. A1. Influence of interface properties on the thermal expansion behavior of generated microstructures without initial cooling: (a) CTE and (b) volume average stresses $\langle\sigma\rangle$ in x,y and z direction.

- the correlation between internal stresses in the components and the CTE behavior was confirmed.
- the dominance of different parameters (e.g. boundary conditions, temperature dependency of properties) in different temperature ranges on the CTE behavior was assigned.

During cyclic cooling, the study found:

- temperature dependency of AlSi10Mg's mechanical properties, internal stresses, and interface detachment induce a cooling peak in the CTE curve at 200 °C after the AlSi10Mg falling below 0.6 $T_m(K)$ absolute melting temperature.
- the peak is shifted to higher temperatures during thermal cycling due to plastic deformation and the changes of internal stresses in the metallic phase.

8. Outlook

Future investigations should serve a better understanding of the underlying effects of the findings and correlations between thermal and mechanical properties obtained in this study. On the one hand, the influence of microstructural changes during heating on the thermal conductivity beyond 100 ×C will be investigated. On the other hand, the correlation of stiffness decrease over thermal cycling in the temperature range up to 500 ×C, by measurement of the elastic modulus via non-destructive methods, as well as the influence of thermal cycling stability on bending strength and fracture toughness should be studied. Finally thermo-mechanical investigations in different temperature ranges and their influence on the lifetime and damage mechanisms will be investigated.

Data availability

The raw/processed data required to reproduce these findings cannot be shared at this time as the data also forms part of an ongoing study.

CRediT authorship contribution statement

Joél Schukraft: Conceptualization, Methodology, Writing – original draft. **Dominik Horny:** Writing – original draft, Software, Formal analysis. **Frederik Siegmund:** Writing – original draft, Investigation, Visualization. **Katrin Schulz:** Writing – review & editing, Supervision. **Kay André Weidenmann:** Writing – review & editing, Supervision.

Declaration of Competing Interest

The authors declare that they have no known competing financial interests or personal relationships that could have appeared to influence the work reported in this paper.

Acknowledgements

The financial support for this work in the context of the DFG research projects SCHU 3074/1-1 and WE 4273/17-1 is gratefully acknowledged. We want to thank Morgan Advanced Materials Haldenwanger GmbH for the friendly supply of complimentary preform material. The numerical parts of this work were performed on the HoreKa supercomputer funded by the Ministry of Science, Research and the Arts Baden-Wõrttemberg and by the Federal Ministry of Education and Research. A special thanks goes to Philipp C. Morbitzer, who was essential in assisting with the in-situ SEM experiments, and to Christopher M. Wünsch and the entire German Aerospace Center, Institute of Test and Simulation for Gas Turbines, for providing the lab and in-situ SEM setup.

Appendix A

References

[1] R. Asthana, A. Kumar, N.B. Dahotre, Materials Processing and Manufacturing Science, Elsevier, 2006.10.1016/B978-0-7506-7716-5.X5000-6
[2] D.K. Koli, G. Agnihotri, R. Purohit, Advanced aluminium matrix composites: the critical need of automotive and aerospace engineering fields, Mater. Today Proc. 2 (4-5) (2015) 3032–3041, https://doi.org/10.1016/j.
[3] M. May, G.D. Rupakula, P. Matura, Non-polymer-matrix composite materials for space applications, Compos. Part C 3 (2020) 100057, https://doi.org/10.1016/j.
[4] T. Huber, H.P. Degischer, G. Lefranc, T. Schmitt, Thermal expansion studies on aluminium-matrix composites with different reinforcement architecture of sic particles, Compos. Sci. Technol. 66 (13) (2006) 2206–2217, https://doi.org/10.1016/j.
[5] J. Broughton, V. Smet, R.R. Tummala, Y.K. Joshi, Review of thermal packaging technologies for automotive power electronics for traction purposes, J. Electron. Packag. 140 (4) (2018), https://doi.org/10.1115/1.4040828.
[6] M.Z. Bukhari, D. Brabazon, M. Hashmi, Application of metal matrix composite of cusic and alsic as electronics packaging materials, in: The 28th international manufacturing conference, pp. 1–9.
[7] C. Hima Gireesh, K. Durga Prasad, K. Ramji, Experimental investigation on mechanical properties of an al6061 hybrid metal matrix composite, J. Compos. Sci. 2 (3) (2018) 49, https://doi.org/10.3390/jcs2030049.
[8] X. Qu, F. Wang, C. Shi, N. Zhao, E. Liu, C. He, F. He, In situ synthesis of a gamma-al2o3 whisker reinforced aluminium matrix composite by cold pressing and sintering, Mater. Sci. Eng. A, 709 (2018) 223–231, https://doi.org/10.1016/j.
[9] A. Mussatto, I.U.I. Ahad, R.T. Mousavian, Y. Delaure, D. Brabazon, Advanced production routes for metal matrix composites, Eng. Rep., 3 (5) (2021), https://doi.org/10.1002/eng2.12330.
[10] K. Lichtenberg, E. Orsolani-Uhlig, R. Roessler, K.A. Weidenmann, Influence of heat treatment on the properties of alsi10mg-based metal matrix composites reinforced with metallic glass flakes processed by gas pressure infiltration, J. Compos. Mater 51 (30) (2017) 4165–4175, https://doi.org/10.1177/0021998317699867.
[11] N. Kota, M.S. Charan, T. Laha, S. Roy, Review on development of metal/ceramic interpenetrating phase composites and critical analysis of their properties, Ceram. Int. 48 (2) (2021) 1451–1483, https://doi.org/10.1016/j.

[12] A. Mattern, B. Huchler, D. Staudenecker, R. Oberacker, A. Nagel, M.J. Hoffmann, Preparation of interpenetrating ceramic–metal composites, J. Eur. Ceram. Soc. 24 (12) (2004) 3399–3408, https://doi.org/10.1016/j.
[13] S. Skirl, M. Hoffman, K. Bowman, S. Wiederhorn, J. Rödel, Thermal expansion behavior and macrostrain of al2o3/al composites with interpenetrating networks, Acta Mater. 46 (7) (1998) 2493–2499, https://doi.org/10.1016/S1359-6454(98)80033-5.
[14] M. Hoffman, S. Skirl, W. Pompe, J. Rödel, Thermal residual strains and stresses in al2o3/al composites with interpenetrating networks, Acta Mater. 47 (2) (1999) 565–577, https://doi.org/10.1016/S1359-6454(98)00367-X.
[15] G.M. La Vecchia, C. Badini, D. Puppo, F. D'Errico, Co-continuous al/al2o3 composite produced by liquid displacement reaction: Relationship between microstructure and mechanical behavior, J. Mater. Sci. 38 (17) (2003) 3567–3577, https://doi.org/10.1023/A:1025613011787.
[16] S. Roy, A. Nagel, K.A. Weidenmann, Anisotropic thermal expansion behavior of an interpenetrating metal/ceramic composite, Thermochim. Acta. 684 (2020) 178488, https://doi.org/10.1016/j.
[17] D.K. Balch, A. Mortensen, S. Suresh, Y.-L. Shen, T.J. Fitzgerald, V.J. Michaud, Thermal expansion of metals reinforced with ceramic particles and microcellular foams, Metall. Mater. Trans. A Phys. Metall. Mater. Sci. 27 (11) (1996) 3700–3717, https://doi.org/10.1007/BF02595462.
[18] Y.L. Shen, Combined effects of microvoids and phase contiguity on the thermal expansion of metal-ceramic composites, Mater. Sci. Eng. A, 237 (1) (1997) 102–108, https://doi.org/10.1016/S0921-5093(97)00121-4.
[19] N.K. Sharma, R.K. Misra, S. Sharma, Modeling of thermal expansion behavior of densely packed al/sic composites, Int. J. Solids Struct. 102-103 (2016) 77–88, https://doi.org/10.1016/j.
[20] O. Lavrentyeva, Verfahren zur herstellung von aufgeschäumten keramischen werkstoffen sowie dadurch herstellbarer keramischer schaum: De, 2016.
[21] D. Horny, J. Schukraft, K.A. Weidenmann, K. Schulz, Numerical and experimental characterization of elastic properties of a novel, highly homogeneous interpenetrating metal ceramic composite, Adv. Eng. Mater. 1901556 (2020), https://doi.org/10.1002/adem.201901556.
[22] P. Mrvar, P. Trbizan, J. Medved, Preiskava dimenzijskih sprememb ulitka in forme med strjevanjem modificiranih in nemodificiranih aluminijevih zlitin z dilatometrom, Livarski vestnik, 48 (5-6) (2001) 131–140.
[23] M. Voncina, P. Mrvar, J. Medved, Thermodynamic analysis of alsi10mg alloy termodinamična analiza zlitine alsi10mg, RMZ Mater. Geoenviron. 52 (3) (2006) 621–633.
[24] J. Schukraft, D. Horny, K. Schulz, K.A. Weidenmann, 3d modelling and experimental investigation on the damage behavior of an interpenetrating metal ceramic composite (imcc) under compressionMater. Sci. Eng. A, (2022) 143147. 10.1016/j.
[25] J. Schukraft, J. Roßdeutscher, F. Siegmund, K.A. Weidenmann, Thermal expansion behavior and elevated temperature elastic properties of an interpenetrating metal/ceramic composite, Thermal expansion studies on aluminium-matrix composites with different reinforcement architecture of sic particles, Compos. Sci. Technol., 66 (13) (2006) 2206–2217, https://doi.org/10.1016/j.
[26] J. Schukraft, C. Lohr, K.A. Weidenmann, 2d and 3d in-situ mechanical testing of an interpenetrating metal ceramic composite consisting of a slurry-based ceramic foam and alsi10mgCompos. Struct., (2021) 113742. 10.1016/j.
[27] Din 51007:2019-04 Thermal analysis - differential thermal analysis (dta) and differential scanning calorimetry (dsc) - general principles, 10.31030/3025544.
[28] E37 Committee, Test method for thermal diffusivity by the flash method, 10.1520/E1461-13R22.
[29] Din 51045, Din 51045-1:2005-08, bestimmung der thermischen längenänderung fester körper_- teil_1: Grundlagen, 10.31030/9636919.
[30] D. Wegscheider, J. Schukraft, K.A. Weidenmann, A metallographic preparation routine for an alsi10mg-al2o3 interpenetrating composite, in: Deutsche Gesellschaft für Materialkunde e.V. (Ed.), Materialography 2022, 2022. https://dgm.de/met/2022/de/programm/wissenschaftliches-programm.A–113
[31] H.W. Swift, Plastic instability under plane stress, J. Mech. Phys. Solids 1 (1) (1952) 1–18, https://doi.org/10.1016/0022-5096(52)90002-1.
[32] R.G. Munro, Evaluated material properties for a sintered alpha-al2o3, J. Am. Ceram. Soc. 28 (8) (1997) 1919–1928, https://doi.org/10.1111/j.1151-2916.1997.tb03074.x.
[33] N.E. Uzan, R. Shneck, O. Yeheskel, N. Frage, High-temperature mechanical properties of alsi10mg specimens fabricated by additive manufacturing using selective laser melting technologies (am-slm), Addit. Manuf., 24 (2018) 257–263, https://doi.org/10.1016/j.
[34] D. Horny, K. Schulz, Analysis of interpenetrating metal ceramic composite structures using an enhanced random sequential absorption microstructure generation algorithm, J. Mater. Sci. 57 (19) (2022) 8869–8889, https://doi.org/10.1007/s10853-022-07180-1.
[35] D.W. Abueidda, A.S. Dalaq, R.K. Abu Al-Rub, I. Jasiuk, Micromechanical finite element predictions of a reduced coefficient of thermal expansion for 3d periodic architectured interpenetrating phase composites, Compos. Struct. 133 (2015) 85–97, https://doi.org/10.1016/j.
[36] Z.H. Karadeniz, D. Kumlutas, A numerical study on the coefficients of thermal expansion of fiber reinforced composite materials, Compos. Struct., 78 (1) (2007) 1–10, https://doi.org/10.1016/j.
[37] Y.L. Shen, Thermal expansion of metal-ceramic composites: a three-dimensional analysis, Mater. Sci. Eng. A 252 (2) (1998) 269–275, https://doi.org/10.1016/S0921-5093(98)00698-4.
[38] GRANTA EduPack, Aluminium a360.0 die cast f.
[39] G. EduPack, Aluminium oxide (99% al2o3)(c-779).
[40] T.W. Clyne, P.J. Withers, An introduction to metal matrix composites, 1st paperback ed., transferred to digital printing, Cambridge University Press, 2003.
[41] GRANTA EduPack, Iron, commercial purity, annealed, (fe).
[42] T. Huber, Thermal Expansion of Aluminium Alloys and Composites, Dissertation, Vienna University of Technology, Faculty of Mechanical Engineering, 2003.
[43] F. Lasagni, G. Requena, B. Mingler, M. Papakyriacou, H.P. Degischer, Entmischung und einformung des si in al–si-legierungen, Sonderb. Prakt. Metallgr., 36 (2004) 443–448.
[44] P. Agrawal, K. Conlon, K.J. Bowman, C.T. Sun, F.R. Cichocki, K.P. Trumble, Thermal residual stresses in co-continuous composites, Acta Mater 51 (4) (2003) 1143–1156, https://doi.org/10.1016/S1359-6454(02)00519-0.
[45] P. Morbitzer, J. Schukraft, C. Lohr, K.A. Weidenmann, In-situ sem investigation on the damage behavior of an interpenetrating metal ceramic compositeCompos. Struct. (in press, 2023).
[46] M.F. Ashby, C. Gandhi, D. Taplin, Fracture-mechanism maps and their construction for f.c.c. metals and alloys. Perspectives in Creep Fracture, Elsevier, 1983, pp. 1–31, https://doi.org/10.1016/B978-0-08-030541-7.50005-9.
[47] L.Y. Jiang, T.T. Liu, C.D. Zhang, K. Zhang, T. Yang, C.C. Zhang, W.H. Liao, Thermal expansion behavior of cnt reinforced alsi10mg composite fabricated via laser powder bed fusion, Mater. Res. Express, 6 (12) (2019) 125806, https://doi.org/10.1088/2053-1591/ab5b5b.
[48] R. Gumbleton, J.A. Cuenca, G.M. Klemencic, N. Jones, A. Porch, Evaluating the coefficient of thermal expansion of additive manufactured alsi10mg using microwave techniques, Addit. Manuf. 30 (2019) 100841, https://doi.org/10.1016/j.
[49] P.S. Turner, Thermal-expansion stresses in reinforced plastics, J. Res. NBS. 37 (1946) 239–250.https://ci.nii.ac.jp/naid/20001326529/
[50] E.H. Kerner, The elastic and thermo-elastic properties of composite media, Proc. Phys. Soc., 69 (8) (1956) 808–813, https://doi.org/10.1088/0370-1301/69/8/305.https://iopscience.iop.org/article/10.1088/0370-1301/69/8/305/meta
[51] R.A. Schapery, Thermal expansion coefficients of composite materials based on energy principles, J. Compos. Mater. 2 (3) (1968) 380–404, https://doi.org/10.1177/002199836800200308.
[52] R.A. Schapery, Stress analysis of viscoelastic composite materials, J. Compos. Mater. 1 (3) (1967) 228–267, https://doi.org/10.1177/002199836700100302.
[53] R.A. Schapery, On the Application of a Thermodynamic Constitutive Equation to Various Nonlinear Materials, 4, Purdue University Report, 1968.